nature biomedical engineering

Article

https://doi.org/10.1038/s41551-025-01367-y

3D-printed perfused models of the penis for the study of penile physiology and for restoring erectile function in rabbits and pigs

Received: 23 October 2023

Accepted: 6 February 2025

Published online: 04 March 2025

Check for updates

Zhenxing Wang[1,2,3,9], Xuemin Liu[4,9], Tan Ye[1,2,3,9], Zhichen Zhai[1,2,3,9], Kai Wu[5], Yudi Kuang[5], Serge Ostrovidov[6], Dan Shao[1,5,7,8], Yingjun Wang[1,2,3] ✉, Kam W. Leong[8] ✉ & Xuetao Shi[1,2,3] ✉

The intricate topology of vascular networks and the complex functions of vessel-rich tissues are challenging to reconstruct in vitro. Here we report the development of: in vitro pathological models of erectile dysfunction and Peyronie's disease; a model of the penis that includes the glans and the corpus spongiosum with urethral structures; and an implantable model of the corpus cavernosum, whose complex vascular network is critical for erectile function, via the vein-occlusion effect. Specifically, we 3D printed a hydrogel-based corpus cavernosum incorporating a strain-limiting tunica albuginea that can be engorged with blood through vein occlusion. In corpus cavernosum defects in rabbits and pigs, implantation of the 3D-printed tissue seeded with endothelial cells restored normal erectile function on electrical stimulation of the cavernous nerves as well as spontaneous erectile function within a few weeks of implantation, which allowed the animals to mate and reproduce. Our findings support the further development of 3D-printed blood-vessel-rich functional organs for transplantation.

The vascular network is an extensive system of blood vessels that spreads throughout all parts of the human body and its vital organs, with the complexity of its network structure enabling it to perform a wide range of tasks[1–4] far beyond the simple transport of oxygen and nutrients[5]. Among these tasks, a unique function is the facilitation of penile erection[6], which depends on the intricate network of blood vessels within the penis. The penis is an organ with one of the most complex vascular network structures in the human body[7]. The penis is primarily composed of three parts: the corpora cavernosa, the corpus spongiosum and the tunica albuginea that covers them[6,8]. Specifically, the corpora cavernosa consists of numerous cavernous spaces, with the cavernous artery of the penis running through the centre of the corpora cavernosa. During erection, the cavernous sinuses expand and compress the venous plexus and the retrosinus vein between the cavernous sinuses, resulting in the blockage of blood flow, swelling of the corpus cavernosum and hyperaemia[9,10], which is necessary to achieve and maintain erection (Fig. 1a). This erection mechanism is often referred to as a type of vein occlusion[11]. When the erection subsides, the blood flow slows and the volume of the cavernous sinus decreases, relieving the compression on the retrosinus vein and the venous plexus, which

[1]National Engineering Research Centre for Tissue Restoration and Reconstruction, South China University of Technology, Guangzhou, P. R. China. [2]School of Materials Science and Engineering, South China University of Technology, Guangzhou, P. R. China. [3]Key Laboratory of Biomedical Engineering of Guangdong Province, South China University of Technology, Guangzhou, P. R. China. [4]The Third Affiliated Hospital, Department of Gynecology and Obstetrics, Guangzhou Medical University, Guangzhou, P. R. China. [5]School of Biomedical Sciences and Engineering, South China University of Technology, Guangzhou International Campus, Guangzhou, P. R. China. [6]Institute of Biomaterials and Bioengineering (IBB), Tokyo Medical and Dental University, Chiyoda, Japan. [7]School of Medicine, South China University of Technology, Guangzhou, P. R. China. [8]Department of Biomedical Engineering, Columbia University, New York, NY, USA. [9]These authors contributed equally: Zhenxing Wang, Xuemin Liu, Tan Ye, Zhichen Zhai.
✉e-mail: imwangyj@scut.edu.cn; kam.leong@columbia.edu; shxt@scut.edu.cn

restores the venous outflow, causing the penis to return to a flaccid state[12]. The process of erection and erection subsidence is similar to the closing and reopening of a valve. Moreover, the tunica albuginea is a tough, white fibrous tissue that encases the entire corpora cavernosa, ensuring that the penis maintains its proper shape and rigidity during an erection[13,14]. However, damage to the corpora cavernosa and tunica albuginea can lead to erectile dysfunction (ED)[7] and Peyronie's disease (PD)[15]. ED is characterized primarily by difficulty achieving an erection, whereas PD involves penile curvature and deformation. The Massachusetts Male Aging Study (MMAS) indicates that the combined prevalence of mild to moderate erectile dysfunction is 52% among men aged 40–70 years, increasing with age. The prevalence of PD is estimated to be between 1% and 13%, and it often coexists with ED[16,17].

Current studies on the physiology and pathology of penile erection are still limited to investigations of actual organs in vivo[8,9,18]. Although recent research on the mechanisms of penile erection has indicated that the cavernosa structure plays an important role in vein occlusion[9,10,12], the interaction of structures and fluids during erection is difficult to observe, and no visual model based on the mechanism of penile erection has so far been established. The complexity of the internal vascular network in the penis and the mechanical challenges caused by the requirement of reasonable deformations during erection make it difficult to construct in vitro models of penile erection.

In this study, a biomimetic physiological model and biomimetic pathological models of the corpus cavernosa of the penis were constructed, and an erection was reproduced in vitro on the basis of the penile erection mechanism. We reconstructed the structure of the complex penile vascular network, made possible by a hydrogel that is compatible with penile erection dynamics and digital light processing (DLP) three-dimensional (3D)-printing techniques. We visualized the interactions of different structures and fluids in typical physiological and pathological erections. On this basis, the construction of the entire penis was further explored.

Recently, there has been a growing emphasis on the development of 3D in vitro functional models for dynamic organs with intricate circulatory networks, such as the heart[19] and alveoli[20]. However, most studies of these dynamic organs in vitro have not been carried out in large animal experiments to further promote their application. In this study, we created a dynamic model of the penile corpus cavernosum that not only reproduced erectile function in vitro but also restored normal penile erect morphology and reproductive function in rabbits and pigs with corpus cavernosum defects generated via in situ implantation. These findings underscore the potential clinical applications of biomimetic corpus cavernosum (BCC) for the treatment of penile injuries. Furthermore, this study advances the clinical application of 3D-printed artificial tissue organs.

Results

Design of the BCC model

On the basis of our analysis of the relationship between the vascular network and erectile function of the penis, we identified, normalized and assembled the major structural components of the corpus cavernosa to create a functional BCC model (Fig. 1a,b). The BCC model can become engorged, similar to a natural erection through vein occlusion. However, because of the mechanical requirements of the matrix material and the complex 3D structure of the model, reproducing an erection in vitro poses several challenges in terms of material selection and preparation technology. In our work, hydrogel ink was chosen for its good printability with a short gel time (Fig. 1c), and the digital light processing 3D-printing method[20,21] (Fig. 1d) was used because of its considerable advantages in the rapid, high-precision manufacturing of complicated structures. The 3D-printing hydrogel ink consists of acrylic acid, gelatin, polyethylene glycol diacrylate (PEGDA, 6 kDa), lithium phenyl-2,4,6-trimethylbenzoylphosphinate (LAP) and tartrazine (Fig. 1d). The hydrogel has an appropriate tensile strength and elastic modulus (Extended Data Fig. 1a), which meet the mechanical requirements for penile corpus cavernosum erection.

The mechanical properties of the hydrogel were crucial for the model's performance. The results of 100 cycles of 50% strain cyclic tensile testing show that the hydrogel has good durability and mechanical stability (Fig. 1e,f), and can recover to more than 90% of the initial maximum stress and dissipate energy after a short relaxation time (Fig. 1g), which matches the erection–flaccidity condition of the penis. To characterize the overall printing accuracy of the BCC model, the BCC model and its internal lumen were investigated via microcomputed tomography (micro-CT) and 3D-reconstruction methods (Fig. 1h and Supplementary Table 1). To visualize the internal structure of the BCC model, we perfused red microfil into the internal lumen of the printed model (Fig. 1i). Specifically, the main components of the designed BCC model are the cavernous artery, arterioles, cavernous sinus, retrosinus vein and venous plexus (Fig. 1b,i).

Numerical simulation analysis was carried out to ensure that the vein occlusion effect was achievable with the BCC model (Extended Data Fig. 2a,b). In this work, we compacted the sinus cavity packing arrangement (Extended Data Fig. 3a) in the BCC model (v.2.0) to increase the proportion of hollow space and achieve a more efficient and substantial deformation response during perfusion (Extended Data Fig. 2c). Thus, the amount of fluid stored in a unit volume in the optimized BCC model (v.2.0) increased (Extended Data Fig. 3b,c), which was more conducive to achieving erection in the cavernosum model in vitro (Extended Data Fig. 2c).

Next, we perfused the model in vitro to mimic the formation and subsidence of an erection of the natural corpus cavernosum (Extended Data Fig. 4). The fluid used for perfusion was a mixture of phosphate buffered saline (PBS) and red blood cells (RBCs, haematocrit to 40%). First, the model was perfused at normal physiological erectile blood flow levels (average flow, 90 ml min^{-1})[22] (Fig. 1j). The high-speed inflow of liquid led to expansion and deformation of the cavernous sinus, and the distances between the edges of the cavernous sinuses were substantially decreased (Fig. 1j and Supplementary Video 1). Numerical simulations were subsequently performed to investigate the perfusion mechanism, and the results revealed that the outflow of fluid through the retrosinus vein was blocked by distension of the cavernous sinus, which compressed the retrosinus vein (Fig. 1k). Subsequently, the perfusion flow rate into the model was reduced to physiological blood flow levels associated with a flaccid state (average flow, 10 ml min^{-1})[22] (Supplementary Video 1). As the retracted cavernous sinus no longer compressed the retrosinus vein, the internal channels of the corpus cavernosum were reconnected to the outside, allowing for unrestricted outflow of fluid. The perfusion mechanism described above illustrates how the BCC model can be guided by perfusion flow to control channel blockage or connectivity, serving as a flow-dependent valve. The 3D-printed BCC model demonstrated the vein occlusion effect under high-speed flow perfusion conditions (90 ml min^{-1}), allowing erections to be achieved and retracted when the fluid flow rate was reduced.

Construction of biomimetic tunica albuginea and a penis model

During the erection, the entire model swelled, but the deformation was uneven; the middle part of the model swelled more than the two ends did (Fig. 1j). This unexpected local deformation is inconsistent with the behaviour of physiological erections. Notably, the large local deformation could easily result in localized damage in the BCC model (Extended Data Fig. 5a), preventing the BCC model from achieving physiological deformation levels during a natural erection under perfusion conditions. To improve our understanding of the deformation and mechanism of the model during the simulated erection process in vitro, we used numerical simulations to calculate the theoretical deformation of the simplified BCC model during perfusion. The numerical

https://doi.org/10.1038/s41551-025-01367-y

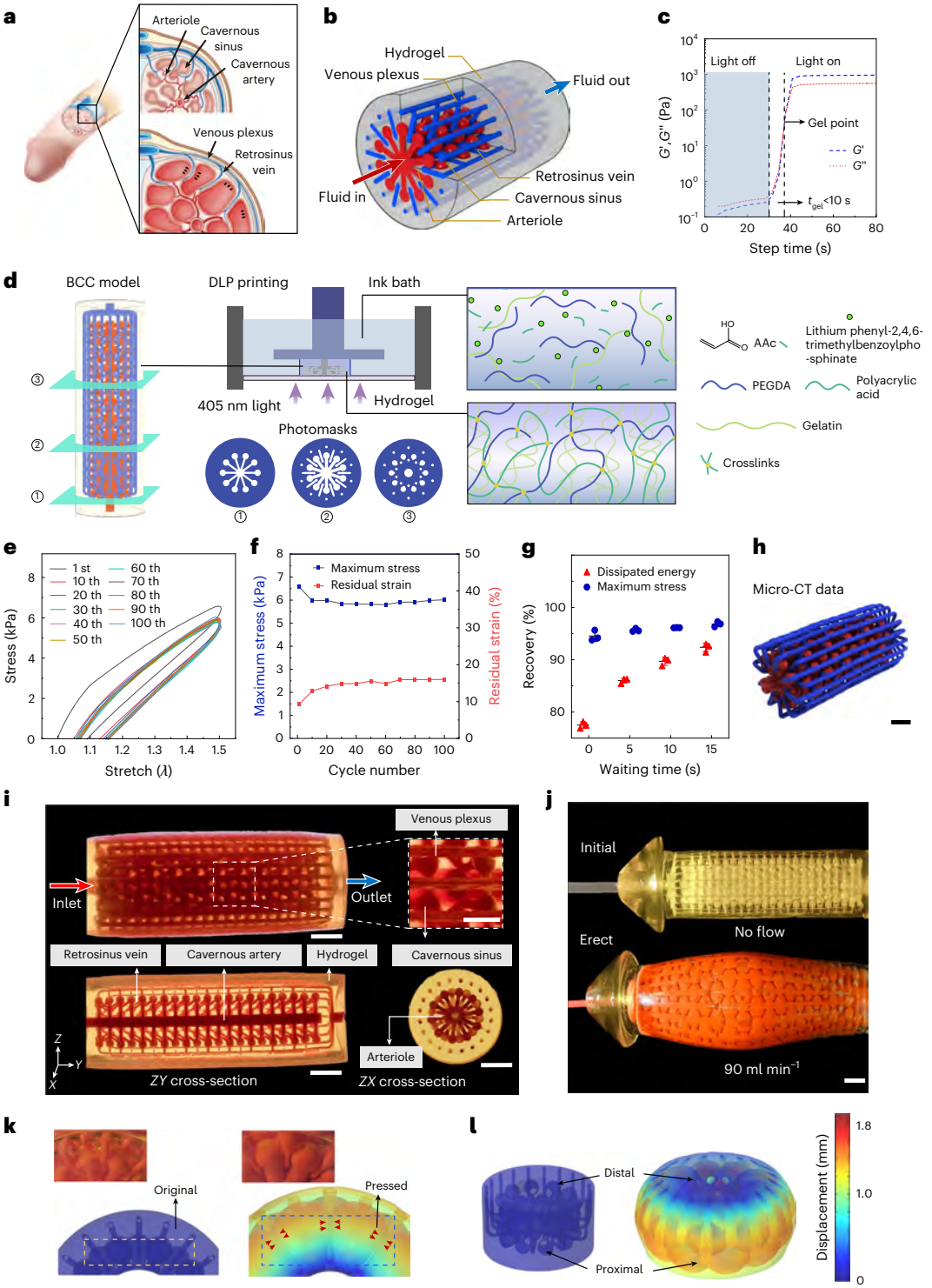

Fig. 1 | Design and construction of a functional biomimetic corpus cavernosum model that achieves vein occlusion. a, Schematic diagram of the erectile mechanism of the corpus cavernosum during erection. The dilated cavernous sinuses compress the retrosinus vein, while the venous plexus impedes blood outflow from the penis, and this process is mimicked by the biomimetic corpus cavernosum (BCC) model. **b**, Structural design of the BCC model. The retrosinus vein in the cavernous sinus in the upper layer passes through the space between the two cavernous sinuses in the lower layer. **c**, Rheology analysis of the hydrogel, showing that the gelation time ($G' > G''$; G', storage moduli; G'', loss moduli) of the hydrogel was less than 10 s. The blue-shaded area indicates the 405-nm light-off state during 0–30 s. **d**, DLP 3D-printing process for the BCC model. **e**, Cyclic tensile loading–unloading curves with a strain of 50%. **f**, Maximum stress and residual strain versus loading–unloading cycle number of the hydrogel. **g**, Recovery ratio of the hydrogel after different relaxation times. **h**, Micro-CT reconstruction of a portion of the BCC model. Scale bar, 2.5 mm. **i**, Photos of the BCC model. In the flaccid state, fluid flows from the cavernous artery, passes through the arterioles, cavernous sinus and retrosinus vein in turn, and finally flows out from the venous plexus. Scale bars, 2.5 mm (magnified top right inset), 5 mm (other three scale bars). **j**, Photos of the BCC model in the initial state and the erectile state during perfusion, showing the increased size of the model during erection. The glans penis-like structure is indicative only and is not perfused. Scale bar, 5 mm. **k**, Numerical simulation results showing compression of the retrosinus vein by the distended cavernous sinuses when the BCC model is in the erectile state. **l**, Perfusion results and numerical calculations showing the overall non-uniform deformation of the model (right: heat map of the displacement of a portion of the model in the flaccid state).

simulation results of uneven local deformation during erection tended to be similar to the experimental results (Fig. 1l).

To address the problems of inconsistent deformation and local damage that occurred during perfusion with the BCC model, we investigated the anatomy of the human penis and found that the tunica albuginea tissue, which wraps around the natural corpus cavernosum, enables control of the deformation behaviour of the penis[13]. The tunica albuginea, which includes an annular layer and a longitudinal layer, is composed of cross-arranged collagen and elastic fibres (Fig. 2a). The high Young's modulus and tensile strength of coiled collagen fibres lead to a strain-limiting effect on the tunica albuginea under extreme strain conditions[23]. In summary, the strain-limiting property of the natural tunica albuginea limits the development of large and localized strains in the corpus cavernosum and ensures that local strains remain at safe levels[24,25].

The natural tunica albuginea structure inspired us to introduce a biomimetic tunica albuginea into the BCC model (Fig. 2b). The biomimetic albuginea is composed of high-tensile-strength fibres (ultrahigh-molecular-weight polyethylene (UHMWPE)), which mimic the collagen fibre network in the natural tissue, coupled with a high-elongation elastic hydrogel that mimics the matrix tissue in the natural tunica albuginea. The biomimetic tunica albuginea wraps around the outer surface of the BCC model, and the lateral fibres and adjacent vertical fibres are connected in an end-to-end manner (Fig. 2c). In this study, we replicated the curled shape of the collagen fibres in the natural tunica albuginea, arranged the UHMWPE fibres in a wavy configuration in the lateral and vertical directions, and embedded the fibres in the hydrogel matrix (Fig. 2c). A sine curve, $y = 1.5 \times \sin(10\pi x/27)$ was selected to control the deformation during erection in the construction of the biomimetic tunica albuginea. The length of this sine curve is 1.5 times its period length, matching the deformation range of the natural corpora cavernosa during erection and effectively simulating the natural physiological deformation process. Uniaxial tensile tests of the biomimetic tunica albuginea in the BCC model revealed a 50% strain limitation effect, typically exhibiting J-shaped stress–strain curves in both the lateral and longitudinal directions (Fig. 2e)[26]. Specifically, before 40% strain was reached, the tunica albuginea exhibited a low modulus and was easily deformed; however, there was a pronounced increase in the modulus between 40–50% strain, followed by a sustained high modulus, resulting in the tunica albuginea becoming resistant to deformation.

In the perfusion experiments, the BCC model first slowly swelled until the fibre network straightened. Next, the model was restricted and underwent more overall deformation while maintaining an erection (Fig. 2d and Supplementary Video 2). The results revealed that the overall deformation of the model was uniform and that there was no excessive local deformation (Fig. 2d,f). After perfusion, the length and diameter of the model reached ~1.45 times and 1.3 times greater than the initial values, respectively (Fig. 2g), approximating the changes that occur during a physiological erection[27,28]. During the expansion of the BCC model, the biomimetic tunica albuginea limited excessive local deformation and prevented damage to the model due to excessive strain. The addition of the biomimetic tunica albuginea led to more consistent overall deformation of the BCC model, reaching normal physiological levels during the simulated erection, with obvious vein occlusion effects (Extended Data Fig. 5b) and maintaining erection for several minutes (Supplementary Video 2). In addition, the intracavernous pressure/perfusion total pressure (ICP/PTP) values were tested via a BL-420 N physiometer by inserting the pressure probe into the tube at the model entrance and exit before and after perfusion. The results were consistent with the trends observed in the physiological ICP/mean arterial pressure (MAP)[29] (Fig. 2h).

Although the corpus cavernosum is the main functional structure involved in erection, the entire penis also includes the corpus spongiosum and the glans penis (Fig. 2i). Here we attempted to develop and construct a full penis model after completing the design and construction of BCC models, which have the potential to replace damaged penis in the future. We preserved the architecture of the biomimetic corpus cavernosum and designed a biomimetic corpus spongiosum and biomimetic glans penis (Fig. 2j); the urethral structures were constructed within the biomimetic corpus spongiosum. We created the biomimetic corpus cavernosa, biomimetic corpus spongiosum and biomimetic glans penis via DLP 3D printing and then combined the parts according to the anatomy of the natural penis (Fig. 2k).

Models to simulate ED and PD

A full mechanistic explanation for erection and pathological erection of the male corpus cavernosum would require a visual model optimized for physiological structure diagnosis, and no such model has currently been developed. Therefore, we altered the biomimetic (physiological) corpus cavernosum model and designed and constructed a model of arteriogenic ED. In vivo, the most common pathology causing arteriogenic ED is atherosclerosis, which is characterized by increased arterial vascular resistance (such as in the penile and cavernous arteries), narrowed blood vessels and decreased arterial blood flow (Fig. 3a)[30]. In this study, we halved the diameters of the cavernous artery and arterioles in the BCC model while maintaining the other structural dimensions to establish an ED model (Fig. 3b). Then, we 3D printed the arteriogenic ED model and perfused it. Regardless of whether the rate of perfusion was low or high, the fluid flowed through the model smoothly (Fig. 3c and Supplementary Video 3). At high flow rates, the total flow rate of the perfusion system in the ED model was the same as that in the BCC model (average flow, 90 ml min^{-1}); however, the reduced diameter of arteries and arterioles led to increased resistance, resulting in decreased branch inflow in the ED model (average flow rate of 50 ml min^{-1}, Extended Data Fig. 5c). This reduced flow caused the model to exhibit no significant deformation or erection (Fig. 3c,d and Supplementary Video 3). Simultaneously, the cavernous sinuses failed to fully expand, limiting the effective compression of the retrosinus vein and the venous plexus. These observations simulate the deformation occurring during perfusion in ED and indicate that atherosclerosis-induced constriction of the cavernous arteries and arterioles may result in ED.

Fig. 2 | BCC model with the developed biomimetic tunica albuginea for controlling deformation during erection. a, Illustration of the mechanism of tunica albuginea stretching during penile erection. As the tunica albuginea stretches, the coiled collagen fibres straighten. **b**, Schematic showing the BCC model wrapped by the biomimetic tunica albuginea. **c**, Structure of the designed biomimetic tunica albuginea. The lateral and vertical fibres are embedded in an elastic matrix (the same hydrogel as in the BCC model). The blue-shaded areas highlight the same fibre in its 'initial' and 'erect' states. **d**, Erectile behaviour of the BCC model with the biomimetic tunica albuginea during perfusion (90 ml min^{-1}), showing homogeneous expansion. Scale bar, 8 mm. The same section of lateral fibres is marked by black dashed boxes in the initial (i) and erect (ii) states. **e**, Uniaxial tensile test results for the different components of the biomimetic tunica albuginea. **f**, Plot of the diameter extension ratio (D_1/D_0) for the BCC model, showing the deformation of the model during erection with (green area) and without (yellow area) restriction from the biomimetic tunica albuginea. **g**, Length (L_1/L_0) and diameter (D_1/D_0) extension ratios of the BCC model with the biomimetic tunica albuginea from the flaccid to the erect state compared with the ratios for normal tissue. Green-shaded areas indicate normal ranges: L_1/L_0 (1.44–1.59) and D_1/D_0 (1.26–1.41). Data are presented as mean ± s.d., $n = 3$ independent replicates. **h**, ICP/PTP values of the BCC model with and without the biomimetic tunica albuginea during erection. Data are presented as mean ± s.d., $n = 3$ independent replicates. Statistical analysis was performed using unpaired two-tailed t-test. NS, not significant. **i**, Schematic showing the anatomy of the penis. **j**, Schematic of the developed full biomimetic penis structure, with blue corresponding to the urethra and red representing the regions of blood flow in the penis. **k**, Images of the full biomimetic penis model. (i), Front view. (ii), Side view. (iii), Partial section view. Scale bar, 3 mm.

https://doi.org/10.1038/s41551-025-01367-y

According to a recent hypothesis, PD is caused by impaired repair of the tunica albuginea after trauma, leading to the accumulation of inelastic scars or plaques. This can result in penile deformities such as curvature, depression, twisting and shortening during erection (Fig. 3e)[15]. On the basis of the locations and mechanical properties of the plaques in biological PD, we created a biomimetic PD model with plaques on the dorsal side. First, a defect was constructed in the central dorsal region of the tunica albuginea in the BCC model equipped with the biomimetic albuginea. Then, the photosensitive resin was dripped onto the defect site and cured to form a coin-shaped plaque with a diameter of 9 mm and a thickness of 2 mm (Fig. 3f,g). The plaque exhibited a much higher elastic modulus (~503.28 kPa) than did the matrix material (~25.03 kPa) (Fig. 3g). We then perfused the biomimetic PD model at normal physiological erectile blood flow levels (average flow, ~90 ml min^{-1}), and we measured the bending angles in the flaccid (θ_1) and erect (θ_2) states. The model transitioned from an initial

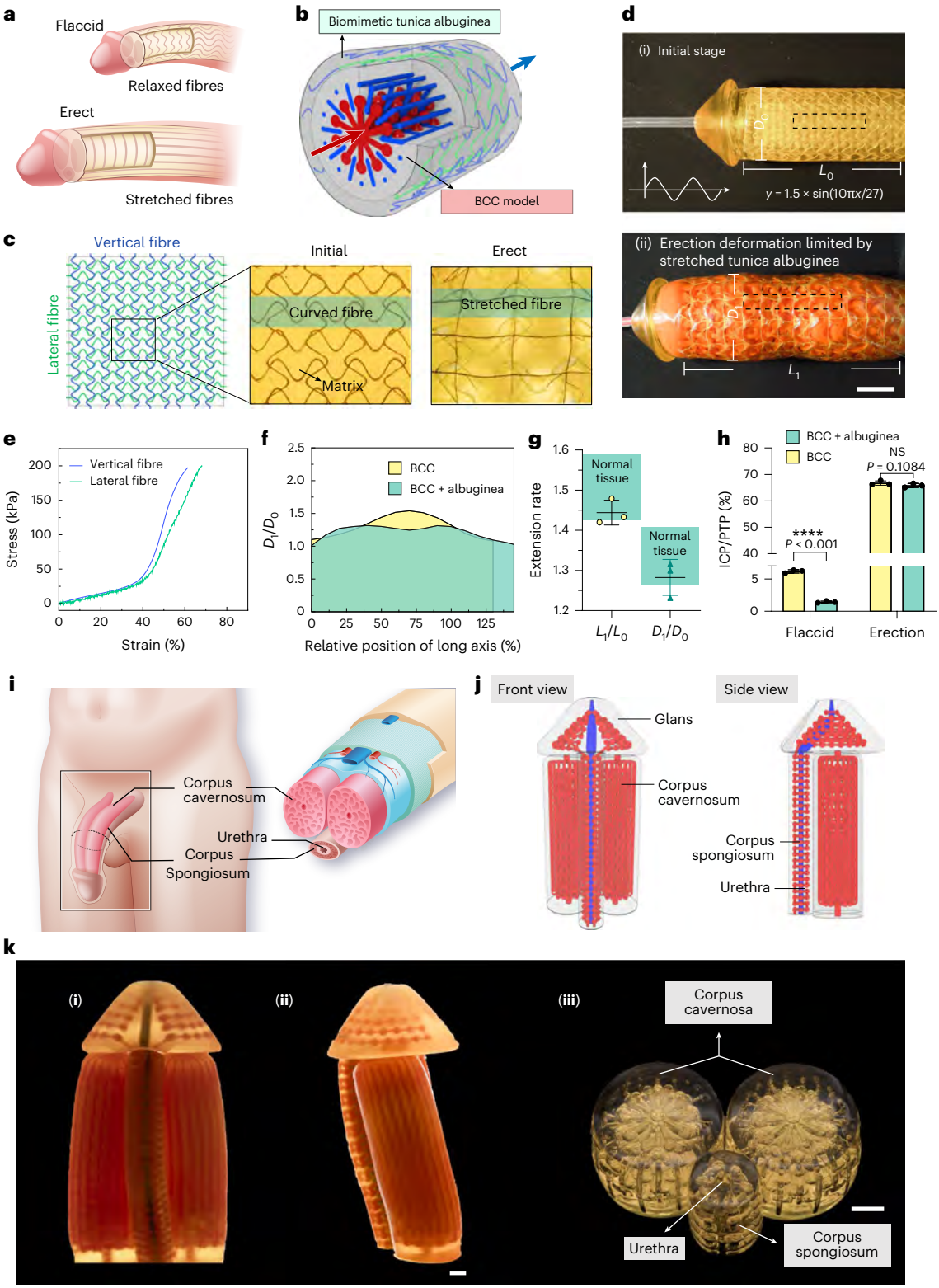

https://doi.org/10.1038/s41551-025-01367-y

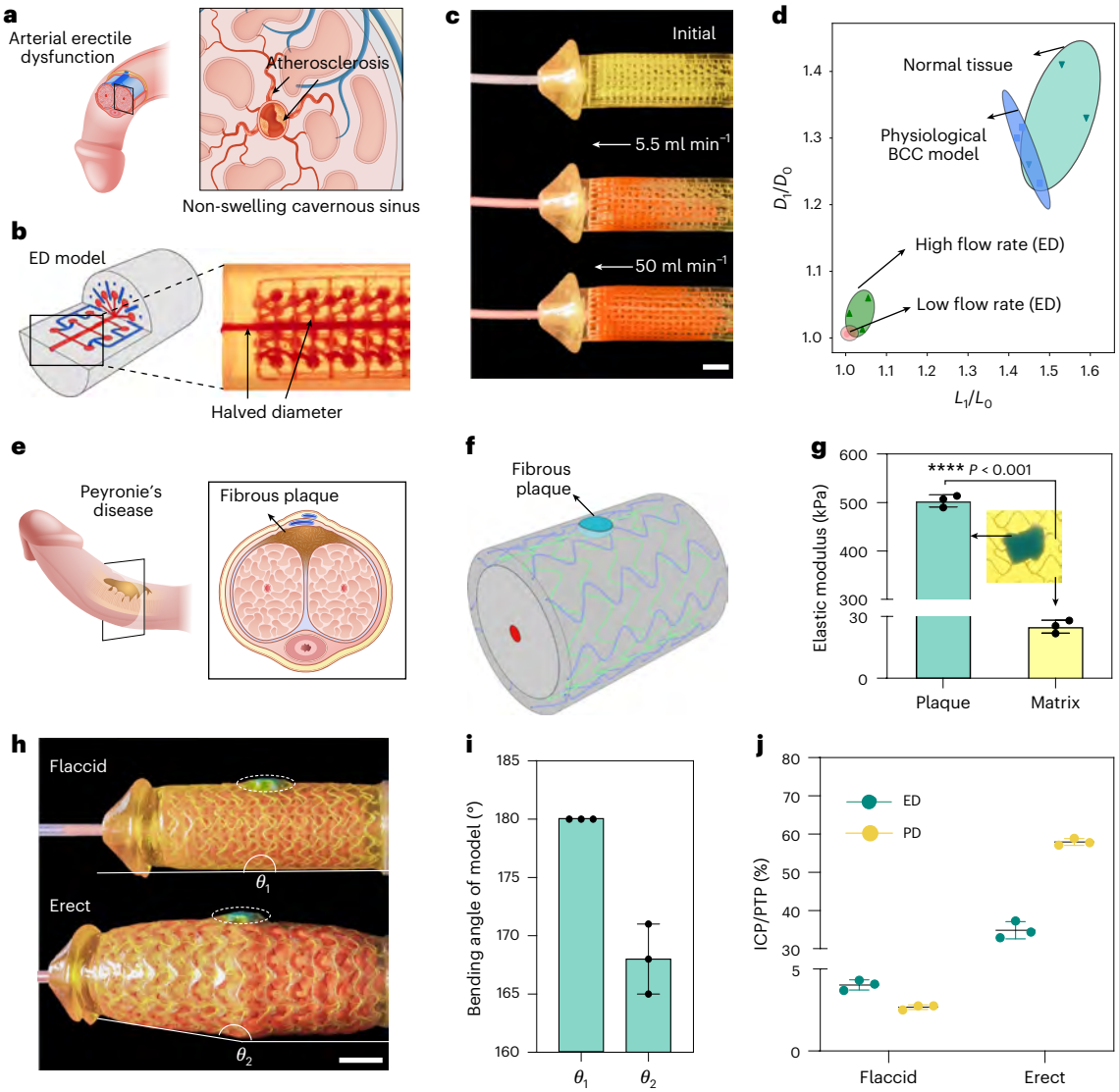

Fig. 3 | Development of pathological BCC models. a, Schematic showing the mechanism of atherosclerosis-induced ED. The cavernous artery and arterioles are confined, hindering full expansion of the cavernous sinuses. **b**, Schematic diagram of the designed arterial ED model. The diameters of the cavernous artery and arterioles are half of those in the physiological BCC model. **c**, Images of fluid perfused into the ED model at low and high flow rates to simulate a pathological erection. Scale bar, 8 mm. **d**, Length ratio (L_1/L_0) vs diameter ratio (D_1/D_0) of the ED model during perfusion at high (50 ml min^{-1}) and low flow rates (5.5 ml min^{-1}) compared with those of normal tissue and the physiological BCC model. **e**, Schematic diagram of a penis affected by PD. Scars or plaques in PD usually occur on the tunica albuginea, especially on the dorsal side of the penis. **f**, Schematic depiction of the PD model, showing a fabricated plaque on the biomimetic tunica albuginea on the dorsal side of the BCC model. **g**, Elastic moduli of the biomimetic tunica albuginea matrix and plaque, $n = 3$ independent replicates. Data are presented as mean ± s.d. Statistical analysis was performed using unpaired two-tailed t-test. **h**, Image of the perfused PD model simulating an erection. The dashed circle indicates the plaque area. During erection, the PD model bends toward the dorsal side because of the difference in elasticity between the plaque and the tunica albuginea. Scale bar, 8 mm. **i**, Bending angles measured with ImageJ software v.1.51j8, $n = 3$ independent replicates. Data are presented as mean ± s.d. **j**, ICP/PTP values obtained during erection in the ED and PD models from measurements with a physiometer, $n = 3$ independent replicates. Data are presented as mean ± s.d.

horizontal state ($\theta_1 = 180°$) to a dorsal curvature state (θ_2 ~165°) (Fig. 3h,i and Supplementary Video 4). The tunica albuginea was hindered from deforming on the dorsal side of the model during the erection because the dorsal side was covered by a plaque with a high elastic modulus. This caused the model to bend toward the dorsal side and mimic clinical PD symptoms. The results of this in vitro experiment demonstrated that low-elasticity scars or plaques might cause the penis to bend to one side during an erection. Finally, we calculated the ICP/PTP values of the ED and PD models before and after perfusion and found that the values were consistent with the trends in the ICP/MAP values for actual pathologies[31] (Fig. 3j). Thus, the PD model simulates the deformation that occurs in PD during perfusion and indicates that the high modulus values of the plaques on the tunica albuginea may result in abnormal angles during erection.

In vitro and in vivo biocompatibility of the BCC model

Given the critical importance of tissue biocompatibility for any implant[32], we thoroughly cleaned the hydrogel matrix to remove residual acrylic acid (Supplementary Fig. 1). In vitro culture of human umbilical vein endothelial cells (HUVECs) and immortalized human aortic smooth muscle cells (IHASMCs) in the hydrogel matrix conditioned medium confirmed its cytocompatibility (Supplementary Fig. 2)[33]. Subcutaneous implantation of the hydrogel in rats showed minimal inflammation at the implantation sites (Supplementary Fig. 3a).

In addition, routine blood analysis indicated that the blood indices of the implantation group remained normal 4 weeks post implantation (Supplementary Fig. 3b,c).

To repair the cavernous defect, we used DLP 3D printing to create a BCC partial model with a sinus cavity structure (Fig. 4a). Then, we seeded endothelial cells (ECs) derived from the corpus cavernosum of pigs or rabbits on the inner wall of the model channels and cultured them in vitro for up to 14 days. After 14 days of in vitro culture, pig ECs and rabbit ECs covered the inner wall of the model channel and formed a fused endothelial layer (Supplementary Fig. 5). These cells maintained their endothelial cell phenotype, characterized by the expression of CD31. The results demonstrate that the BCC partial model having good biocompatibility can support the long-term and stable adhesion of ECs in vitro, laying the foundation for the in vivo implantation of the corpus cavernosum model with cells seeded on the inner wall of the channels. The presence of ECs is important for the cavernous sinus structures of models that are in direct contact with blood.

Engineered implants for corpus cavernosum repair in rabbits

We conducted in vivo implantation experiments aimed at repairing the corpus cavernosum defects in rabbits. For the implantation group, we treated the model surface with heparin to prevent coagulation (Supplementary Fig. 4)[34]. For the ECs + implantation group, we seeded the inner wall of the model channel with rabbit ECs expressing mCherry fluorescent protein (abbreviated as mCherry$^+$ ECs (red)) (Supplementary Fig. 5). We created defects in the corpus cavernosa of male rabbit penises and implanted a model into these rabbits to address the cavernosum defects (Fig. 4a and Supplementary Fig. 6).

Twelve weeks after surgery, we conducted measurements of the ICP and MAP across different experimental groups under identical electrical stimulation of the cavernous nerve. The ICP/MAP ratio was employed as an indicator of erectile function restoration (Fig. 4b). After a 12-week recovery period, the results showed that the defect group presented the lowest ICP/MAP ratio (0.272 ± 0.019), while the implantation group showed a significant improvement (0.494 ± 0.022). The ratio in the ECs + implantation group (0.675 ± 0.015) further increased, approaching that in the normal group (0.748 ± 0.029). These findings indicate that the implants markedly improved functional recovery, and the combination with ECs further enhanced this effect, demonstrating notable improvements in tissue regeneration and functional recovery.

Magnetic resonance imaging (MRI) was subsequently utilized to observe and evaluate the structural integrity of the rabbit corpus cavernosum at 4 and 12 weeks post implantation (Fig. 4c). The 4-week repair of the rabbit corpus cavernosum was limited, with all groups showing noticeable defects in the MRI images (Fig. 4c and Supplementary Fig. 6). After 12 weeks, the structure of the corpus cavernosum was essentially restored in the ECs + implantation group, with a morphology similar to that of the normal group. Furthermore, compared with the control group, the implantation groups (without ECs) presented a substantially smaller scar area, suggesting that the implantation is beneficial for the regeneration of the cavernous tissue (Fig. 4c).

The in vivo imaging results demonstrated notable cell retention at both 4 and 12 weeks post operation, with the fluorescence signal intensity decreasing over time and showing slight diffusion (Fig. 4d). Immunofluorescence staining revealed the presence of exogenous mCherry$^+$ ECs (red) at 4 and 12 weeks post transplantation. In addition, the exogenous ECs were notably integrated with endogenous CD31$^+$ vascular ECs to form new sinus structures (Fig. 4e). After 10 weeks, the male rabbits were mated with females for 2 weeks (Fig. 4f,g). Birth rates were recorded (n = 5 rabbits). Within a 4-week period, 4 female rabbits in the ECs + implantation group and 5 female rabbits in the normal group delivered offspring (Fig. 4h). In contrast, only one female in the control group gave birth to offspring during the same period (Fig. 4h). The fertility of the EC groups demonstrates the recovery of erectile function and the ability to ejaculate, suggesting the restoration of the cavernous tissue in the treated males.

Engineered implants for porcine corpus cavernosum defects

Furthermore, we have expanded our research on repairing corpus cavernosum defects to large animals. The BCC partial model containing sinus cavity structures was again constructed via DLP 3D printing (Fig. 5a). For the implantation group, we also treated the model surface with heparin to prevent coagulation. For the ECs + implantation group, we seeded the inner wall of the model channel with mCherry$^+$ pig ECs (red). We created defects in the corpus cavernosa of male Bama pigs, implanted the model into pigs with cavernosum defects and sutured the incision (Fig. 5a and Extended Data Fig. 6a).

Two weeks after surgery, the erection was induced by electrical stimulation of the nerves, and the erection morphology showed that the corpora cavernosa of pigs exhibited varying degrees of engorgement, which could last up to 60 s. The ECs + implantation group and the implantation group achieved normal erection in terms of the erection morphology (Fig. 5b). However, in the defect group, the erection was abnormal due to a noticeable angle at the injury site (Supplementary Fig. 7). The blood flow determined by colour Doppler ultrasound showed no significant differences among the different groups during the erect state (Supplementary Fig. 8). Overall, the results demonstrated that a corpus cavernosum model can momentarily restore a partially defective penis to its normal erectile morphology.

The MRI results indicated that penile repair in the ECs + implantation group was comparable to that in the normal group, while the implantation group showed better structural repair than the defect group did (Supplementary Fig. 9). At 4 and 8 weeks post operation, in vivo imaging demonstrated obvious cell retention (Fig. 5c). Frozen tissue sections revealed that the transplanted fluorescent protein-expressing cells were well integrated with the surrounding corpus cavernosum tissue (Fig. 5d and Supplementary Fig. 10), supporting the role of ECs in corpus cavernosum regeneration. Haematoxylin and eosin (H&E) and Masson staining of penile tissue post implantation revealed low inflammation levels in the implantation groups at 4 and 8 weeks, with new tissue progressively forming as the model degraded at the defect site (Fig. 5e and Supplementary Fig. 11). Compared with the implantation group, the ECs + implantation group presented faster tissue regeneration and sinus structures formation. These findings indicate that the combination of implants and ECs considerably enhances the regeneration of corpus cavernosum defects.

The RNA-sequencing results also confirmed the neogenesis and low inflammation of the tissue near the defect site in the implantation group 8 weeks after implantation (Extended Data Fig. 7a,b, and Supplementary Figs. 12 and 13). Furthermore, it was also confirmed that compared with the implantation group, the ECs + implantation group had better angiogenesis and tissue neogenesis, and lower inflammation levels (Supplementary Fig. 14a–c). Routine blood analysis indicated that after 4 and 8 weeks, the porcine blood indices in the implantation group were normal (Extended Data Fig. 6b,c).

The pregnancy rates were assessed via ultrasound imaging after mating (Fig. 5f,g). The defect group had the lowest pregnancy rate, at only 25%, indicating poor reproductive function recovery without any intervention. The implantation group showed a remarkable improvement in the pregnancy rate to 75%, suggesting that the implants had a positive effect on reproductive function recovery. The ECs + implantation group achieved a 100% pregnancy rate, with all female pigs becoming pregnant, demonstrating the strong ability of ECs combined with implants in promoting reproductive function recovery (Fig. 5h and Supplementary Fig. 15).

Discussion

The vascular architecture of the penis and the role of vein occlusion in the regulation of erections have been the subject of extensive

https://doi.org/10.1038/s41551-025-01367-y

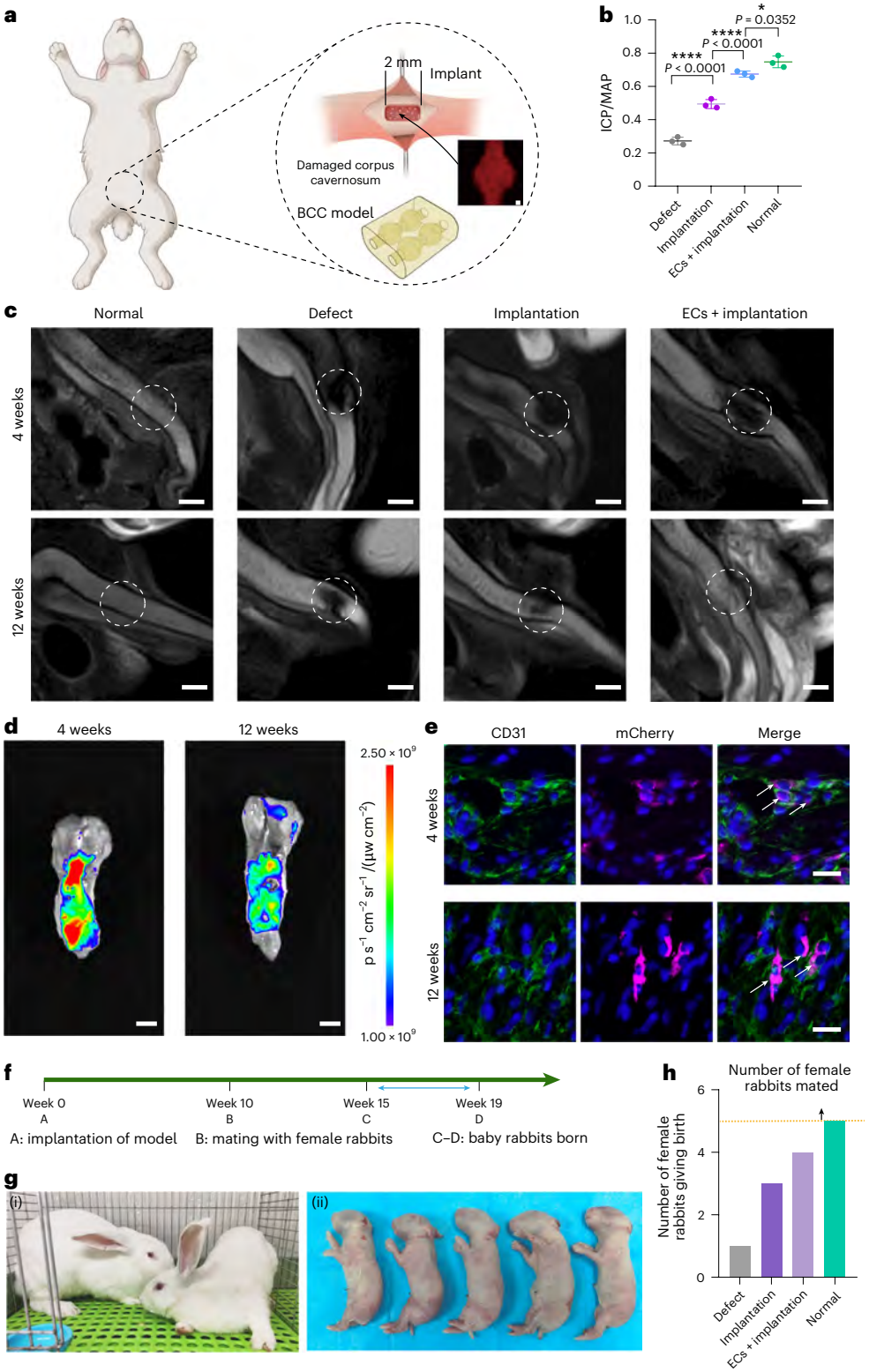

Fig. 4 | Model for repairing defects in the rabbit corpus cavernosum. **a**, Schematic diagram of the procedure for implanting the model into a defect made on the rabbit corpus cavernosum. The inner sinus wall of the model is covered with mCherry$^+$ ECs (red). Scale bar, 100 μm. **b**, The ICP/MAP value was recorded after 12 weeks of implantation. Data are displayed as mean ± s.d. (n = 3 rabbits) and analysed using GraphPad Prism software via one-way analysis of variance (ANOVA). ECs + implantation vs normal *P = 0.0352. **c**, MRI images of 4 different groups: defect, implantation, ECs + implantation, and normal cavernosum (normal). The scar areas are marked with a white circle and were observed at 4 and 12 weeks after implantation. Scale bar, 20 mm. **d**, Live imaging of mCherry$^+$ ECs on the models in rabbits after 4 and 12 weeks of implantation. The colour bar represents radiant efficiency. Scale bar, 5 mm. **e**, Immunofluorescence images of mCherry$^+$ ECs (magenta) and the CD31 (green) and DAPI staining (blue), and their co-localization (indicated by white arrows) in corpus cavernosa tissue of rabbits at 4 and 12 weeks after transplantation. Scale bar, 20 μm. The experiments were independently repeated 3 times with similar results. **f**, Timeline of mating experiment steps. **g** (i), The ECs + implantation group mating with female rabbits. (ii), Newborn baby rabbits. **h**, The numbers of female rabbits that gave birth to newborn rabbits in different groups during the mating assessment test.

https://doi.org/10.1038/s41551-025-01367-y

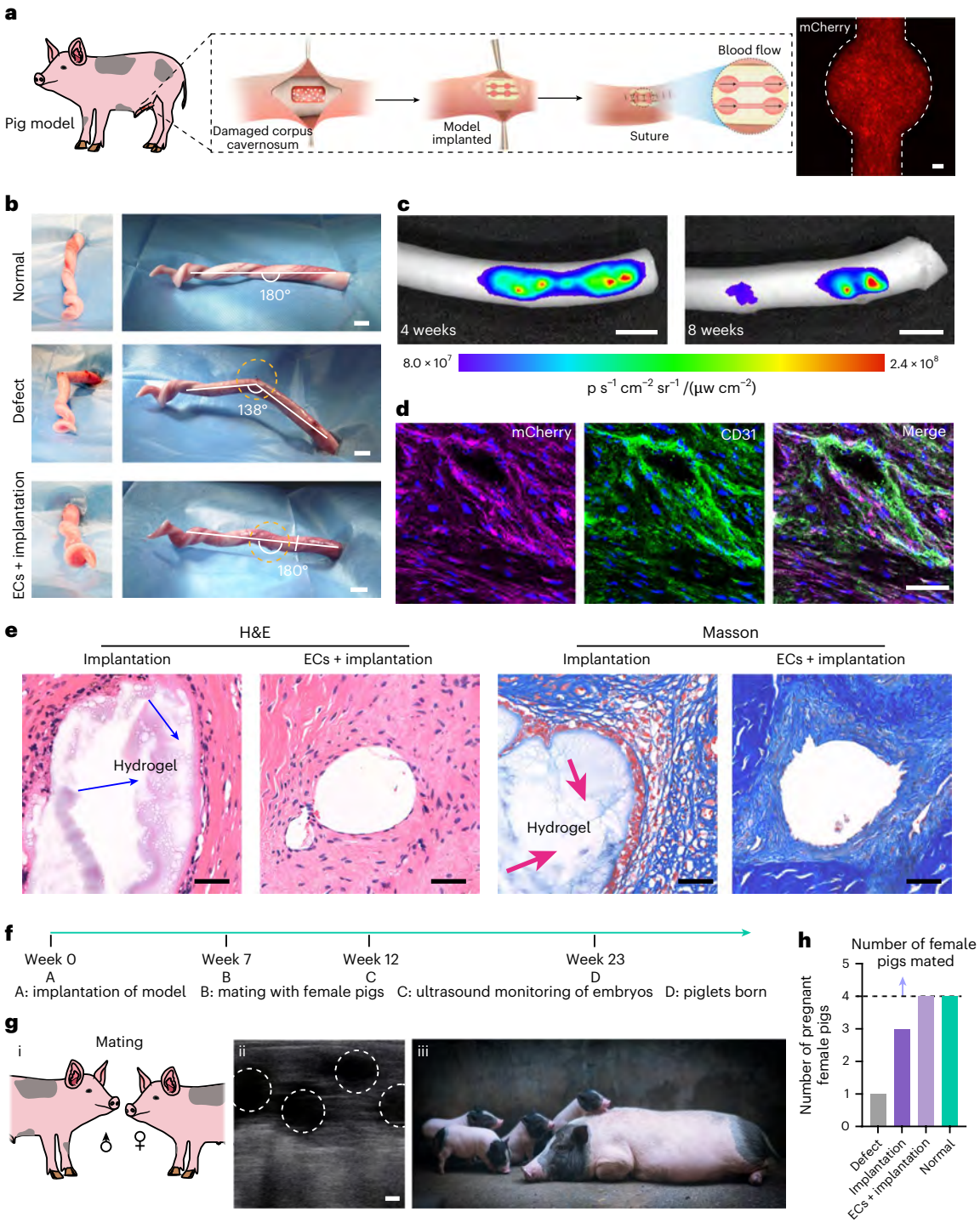

Fig. 5 | Model for repairing defects in the pig corpus cavernosum. a, Schematic diagram of the procedure for implanting the model into a defect made on the porcine corpus cavernosum. The inner sinus wall of the model is covered with mCherry$^+$ ECs (red). White dashed lines outline the model channels. Scale bar, 100 μm. **b**, The erection of porcine penises was induced by electrical stimulation of the nerves. Two weeks after implantation, the implanted model allowed recovery of a normal penis shape in pigs with corpus cavernosum defects during erection. Orange circles indicate the surgically created defect sites. Scale bar, 10 mm. **c**, Live imaging of mCherry$^+$ ECs on the models in pigs 4 and 8 weeks after implantation. The experiment was repeated independently 3 times. The colour bar represents radiant efficiency. Scale bar, 10 mm. **d**, Fluorescence imaging of CD31 (green) and mCherry$^+$ cells (magenta) in corpus cavernosum sections 8 weeks post implantation. The experiment was repeated independently 3 times. Scale bar, 50 μm. **e**, Histopathological examination (H&E and Masson's trichrome staining) of corpus cavernosum sections 8 weeks after implantation. Scale bar, 300 μm. **f**, Timeline of the mating experiment steps. **g** (i), The implantation group mating with female pigs. (ii), Ultrasound of embryos (white circles indicate embryo positions). Scale bar, 10 mm. (iii), Newborn piglets. **h**, The numbers of pregnant female pigs in different groups during the mating assessment test.

research[8–10,12,18]. However, constructing a biomimetic vascular network structure of the corporal model to achieve dynamic erectile function still poses challenges in terms of materials, structural biomimetic design and manufacturing methods.

The hydrogel used in this study is strong enough to withstand the pressure of an erection. Its lower elastic modulus, ~25.03 kPa, renders the model highly conducive to achieving an extensive strain exceeding 1,400% (Extended Data Fig. 1a) that spans the needed strain range (≤50%). In comparison with commonly used hydrogels such as gelatin methacryloyl (GelMA)[35], PEGDA[36] and several others[37–41], the hydrogel we used showed superior performance because of its excellent combination of high strength, substantial strain tolerance and low elastic modulus (Extended Data Fig. 1b,c). Moreover, it also exhibits favourable characteristics in terms of photocurable printing performance (Extended Data Fig. 1d) and biocompatibility. This hydrogel is poised to find wide-ranging applications in the construction of intricate structures, including models of soft tissues or organs that undergo substantial deformation.

With an optimized hydrogel, we have pioneered the construction of a BCC model with an embedded complex vascular network, where erection can be controlled through perfusion flow. The model provided forward guidance for artificial vessel-rich organs. The unique dynamic erection deformation behaviour of the BCC model consistent with the physiological level of the penis was first achieved in vitro through the vein occlusion effect via the synergy generated by biomimetic multistructures, which may inspire the creation of dynamic behaviours of organs (for example, the heart and the lungs) from structure to function. Currently, mimicking dynamic organs involves overcoming considerable challenges, including replicating the complex structural features, mechanical properties and functional responses of these organs. Taking the heart and alveoli as examples, the unique structure of the heart, consisting of four chambers and valves, ensures unidirectional blood flow. The myocardium and the electrical conduction system of the heart guarantee continuous, rhythmic contractions. Alveoli have extremely thin walls and are supported by a network of capillaries, bringing the air in the alveoli very close to the blood, forming an alveolar–capillary interface for efficient gas exchange.

Our study also involved structural optimization of the BCC model. Through numerical simulation, the deformation of the BCC model can be predicted in advance, allowing for adjustment and optimization of its structure. In addition, inspired by the strain-limiting effect of the natural tunica albuginea, we used a biomimetic tunica albuginea to address the issue of non-uniform local deformation of the BCC model during perfusion. Under the constraint of the biomimetic tunica albuginea, the BCC model achieved erectile deformation equivalent to that observed physiologically via vein occlusion. In the future, the wavy elastic fibre network in the biomimetic tunica albuginea could be reconfigured to achieve programmable and precise deformation limitations for flexible sensors[42,43] and soft robotics[44].

We constructed arterial ED and PD models as visual and analytical tools to investigate pathological erections and penile structural abnormalities. The BCC model features a biological valve structure responsive to flow variations in the corpus cavernosum. This valve could be used to create a type of valve that automatically causes obstructions under high-flow conditions and promotes circulation under low-flow conditions. Unlike conventional valves, it can block or connect on the basis of liquid flow driving the valve to squeeze the backflow channel. Thus, our BCC model is applicable not only as a biomimetic design for an artificial penis but also for developing a valve for controllable flow-induced occlusion, with potential use in interventional surgery as a temporary embolization device.

The BCC model serves as both an in vitro visualization tool and an advanced solution for cavernous repair. Pioneers used decellularized extracellular matrix with endothelial cells to restore cavernous defects[8,45] but faced challenges with non-customizable sinus structures and limited donor availability. Our approach integrates biomimetic sinus structures, personalized defect repair via 3D printing, and both short-term support and long-term functional restoration, offering a more sophisticated solution for cavernous defect repair.

These outcomes underscore the substantial clinical prospects of the generated BCC model for remedying corpus cavernosum defects and enabling penis transplantation, thereby establishing promising avenues for medical applications in this domain[34]. Furthermore, they advance the clinical transplantation of 3D-printed artificial tissue organs.

In summary, we used a model of partial corpus cavernosum dysfunction to assess whether an implant possessing biomimetic structural characteristics and seeded with endothelial cells can promote penile function recovery. Although promising, this approach has limitations when it comes to regenerating and repairing large-scale penile injuries. Notable damage to the corpus cavernosum can involve injury to nerves, the urethra and the complex vascular networks within the tissue. Currently, developing transplant materials that support nerve regeneration and effectively integrate with the host's urethra and vascular networks presents a major challenge. To address these issues, future research could explore design strategies aimed at inducing nerve regeneration and embedding artificial blood vessels and urethral structures within the implants. In addition, the endothelial cells differentiated from autologous pluripotent stem cells (iPSCs), which have high expansion potential, can replace the resource-constrained exogenous endothelial cells seeding the transplant site, thereby further minimizing immunogenicity. Moreover, advanced 3D-printing techniques such as two-photon printing could be used to achieve spatially specific arrangements of different cell types, allowing for the construction of biomimetic models with specific microstructures. These approaches could help overcome current obstacles in repairing large-scale penile injuries.

Methods

Materials

The printing ink used to construct the BCC model consisted of 30% (w/w) acrylic acid, 10% (w/w) gelatin, 2.5% (w/w) PEGDA (6 kDa), 0.5% (w/w) LAP and 0.1% (w/w) tartrazine dissolved in deionized water, and was stored at 4 °C in darkness. PEGDA was prepared as follows. Briefly, dry polyethylene glycol (PEG) (3 mmol), triethylamine (9 mmol) and acryloyl chloride (9 mmol) were dissolved in 180 ml of anhydrous dichloromethane and reacted for 24 h under argon gas. The yield was 80% and the percentage of arylation was ~90%. These results were verified by ^{1}H nuclear magnetic resonance (NMR) spectroscopy, identifying the characteristic peak of the PEG methylene proton adjacent to the acrylate (Supplementary Fig. 16).

Design and construction of the BCC model

The model structure was designed in Blender (Blender Foundation, Amsterdam, the Netherlands). We iteratively optimized several versions of the BCC model to achieve vein occlusion during the erection process. In each version, the cavernous artery was placed at the centre of the model, and the basic structural unit included the small artery, cavernous sinus and posterior sinus vein. The underlying unit structures were arrayed linearly and equidistantly along the z axis, and several retrosinus veins from the array were connected to a single venous plexus to generate a collection of unit structures. Then, arrays of cavity units were formed by rotating the units by equal angles (36°) 10 times and connecting all the venous plexuses to the outlet to obtain the solid structure of the internal duct of the model. Finally, we performed Boolean subtraction on the basis of the perusable ducts in the solid cylinder (Φ = 16 mm) to generate the final 3D-printed model (Extended Data Fig. 3a).

To compare the volume of the internal pipeline cavity for different BCC models after normalization, we proposed the concept of the hollow ratio (R_h), expressed in equation (1) as follows:

$$R_h = \frac{V_p}{V_c} \times 100\% \quad (1)$$

where V_p is the volume of the internal pipeline cavity for each model version and V_c is the volume of the external cylinder for each model version.

The structural design process of the ED model was similar to that of the abovementioned BCC model, with the only difference being the size settings of some structures. Specifically, in the ED model, the diameters of the cavernous artery and arterioles were half of the corresponding diameters in the BCC v.2.0 model. The PD model was modified and formed on the basis of the BCC v.2.0 model wrapped with the biomimetic tunica albuginea. As mentioned in the main text, the tunica albuginea in the PD model was designed with a hard plaque in the centre. The overall size of the BCC model is 62.5 × 16.8 mm (length × diameter, including the glans penis-like structure, 12.5 mm in length). It is designed to be close in size to a normal human penis. In addition, the diameter of the sinus cavity set in the model is 1.6 mm.

The parameters employed to construct the BCC model using a DLP 3D printer (Bio-Architect WS, Regenovo) were as follows: an optical machine resolution of 50 µm, a slice thickness of 50 µm and an exposure of 15 s per layer (20 mW cm^{-2}) at room temperature.

Characterization of the BCC model

To visualize the internal structure of the BCC model, we perfused red microfil (Flow Tech) into an internal channel in the printed model. After the microfil had cured inside the cavity, macrophotos of the BCC model were acquired with a camera (a6300, Sony) and a macro lens (Art 70 mm, SIGMA) in RAW mode (24 megapixels) under indoor lighting conditions or with a camera light (SL60 W, Godox). Videos were acquired with the same equipment.

Since microfil contains a radiopaque component, we used micro-CT to determine the printing accuracy of the BCC model. A micro-CT scanner (SkyScan 1272, Bruker) was used to scan the microfil-perfused BCC model at a 100-µA scan current, 7-W power, 100-ms exposure time and 25-µm voxel resolution as the model was rotated on its long axis once. The internal topography of the BCC model was visualized by importing the reconstructed images into Mimics image analysis software (Materialise) and marking the arterial and venous segments of the model with different colours.

Perfusion device

To achieve an erection, we perfused fluid into the models developed in this study, including the physiological and pathological models (ED and PD) described above. The device used to perform the perfusion mainly consisted of a reservoir bottle, peristaltic pump, fixation frame and model body. These parts were linked by a sequence of silicone tubes and connectors to form a pipeline circuit (Extended Data Fig. 4). Among these parts, the root of the model body and the fixed frame were light cured and bonded using the aforementioned printing ink without tartrazine; the inlet joint on the fixed frame coincided with the inlet of the model body. Typically, after initiating the infusion, the liquid from the reservoir bottle flowed into the model body under the drive of the peristaltic pump and out of the model body via the model outlet back into the reservoir bottle. An ultrasonic flowmeter (FD-XS8, Keyence) was used to detect instantaneous flow rate information in the perfusion pipelines.

Computational modelling

The COMSOL Multiphysics parameters were configured as follows. First, to reduce the number of operations, the BCC model was simplified: as the model was symmetric about the central axis, one-quarter of the original model was extracted, and three layers of characteristic units were extracted from the original model and studied. Then, for the solid mechanics analysis, we set the Young's modulus of the material to 27 kPa, the Poisson's ratio to 0.49 and the density to 1,390 kg m^{-3} based on the aforementioned characterization of the mechanical properties of the BCC material. Next, for the fluid mechanics analysis, since the density and dynamic viscosity of the fluid used in the perfusion experiments are similar to those of human blood, we set the fluid density to 1,060 kg m^{-3} and the dynamic viscosity to 5 × 10^{-3} Pa × s. For the boundary conditions, we set the inlet flow velocity as 0.8 m s^{-1}, the top surface of the model as a fixed constraint and the two rectangular sides of the model as symmetric boundary conditions. Finally, we chose a direct linear equation solver and a fully coupled nonlinear system of equation solvers for the numerical calculations.

Preparation of the biomimetic tunica albuginea

Blender software was used to design the biomimetic tunica albuginea, which had dimensions of 53.5 × 52 × 2 mm (length, width and thickness) and included 13 equally spaced sine curve grooves on the top surface and 10 symmetric sine curve grooves on the bottom surface. The grooves were made by sweeping a 0.75 × 0.3 mm (height and width) rectangle along a sine curve, with the starting point at the centre of the rectangle, and subtracting the result from the main body. The sine curve equation was formulated as follows:

$$y = 1.5 \sin\left(\frac{10\pi}{27}x\right) \quad (2)$$

where y represents the vertical displacement (mm), and x represents the horizontal distance (mm). The designed biomimetic tunica albuginea model was imported into DLP 3D-printer software for printing. The printing ink and printing parameters were the same as those used in the construction of the BCC model. The printed model was rinsed with deionized water to remove residual ink inside the grooves. Then, 0.15-mm-diameter UHMWPE fibres were buried in the grooves of the printed model, and 20-mm threads were reserved at the beginning and end of each groove for subsequent fibre knotting. Finally, the completed model was cured and crosslinked at 405 nm for 240 s to obtain the final biomimetic tunica albuginea.

The biomimetic tunica albuginea was wrapped around the outer surface of the BCC model, the lateral fibres were tied in an end-to-end manner, and the adjacent vertical fibres were connected in head-to-head and tail-to-tail manners. Then, the joint of the biomimetic tunica albuginea was filled with tartrazine-free printing ink and irradiated at 405 nm for 30 s for cross-linking to cure the joint.

Photorheology characterization

Photorheological characterization of the hydrogels was performed using a rheometer (Discovery HR-2, TA) equipped with a 20-mm-diameter parallel plate geometry and optical accessories with a light source wavelength of 405 nm. For each sample, the pre-hydrogel mixture (ink) was dropped onto the bottom plate, and the top test plate was lowered to obtain a gap size of 50 µm. A 150-s time sweep was performed with an angular frequency of 5 rad s^{-1} and a strain of 10%, in which the sample was pretreated for 30 s, and then 405-nm light irradiation was sustained for 120 s, with an optical power density of ~20 mW cm^{-2}.

Mechanical tests

For the uniaxial tensile tests, the printing ink for all the models and the photosensitive resin used to construct the biomimetic PD model plaque were poured separately into the tension specimen mould and irradiated at 405 nm for 240 s. After demoulding, a tension specimen with a size of 41 × 18 × 2 mm (length, width and thickness) was obtained. The tension specimen for the biomimetic tunica albuginea was prepared via the same procedure as that used to create the entire tunica albuginea. The stretching strips were classified into two types on the basis of whether they were stretched longitudinally or transversely. Each stretching strip contained four lateral UHMWPE fibres and three vertical UHMWPE fibres, which was approximately the same ratio of

lateral to vertical fibres as in the entire biomimetic tunica albuginea. Uniaxial tensile tests were performed using a universal testing machine (Instron 5967, Instron) at a speed of 30 mm min^{-1} at room temperature.

A dynamic mechanics analyser (Q800, TA) was utilized for the cyclic loading–unloading tensile tests, and the strain rate was 200% min^{-1}. The area of the hysteresis loop could be used to calculate the energy dissipation.

Erection deformation and uniformity test

In the recorded perfusion video, images were captured at the start and at full erection (at the start of and after 30 s of low-speed (5.5 ml min^{-1}) and high-speed (50 ml min^{-1}) perfusion measured by the ultrasonic flowmeter for the biomimetic ED model) and imported into ImageJ v.1.51j8 software to determine the length and diameter of the models.

In the recorded perfusion videos of the BCC model with and without the wrapped biomimetic tunica albuginea, the images at the start and at full erection were captured and imported into ImageJ software. The root of the model was taken as the origin, and the percentage of the original length of the model in the direction of the long axis was plotted on the *x* axis. The diameter at each coordinate point when the model was fully erect was measured.

ICP test method

To determine the internal pressure during perfusion for all models (including the BCC, BCC with the wrapped biomimetic tunica albuginea, ED and PD models), one pressure probe of a physiometer (BL-420 N, Techman) was inserted into the tube at the model entrance, and the other probe was inserted into the model exit. Then, the perfusion device was turned on and the internal pressure of the model during the perfusion process was recorded.

For inducing penile erection via electrical stimulation in male rabbits or Bama pigs, the following procedure was employed: after anaesthesia, male rabbits (or Bama pigs) were placed in a supine position. The mean arterial pressure was measured using a PE-50 tube connected to a 3-way stopcock inserted into the carotid artery. A 23-gauge needle attached to a sensor was inserted into the corpus cavernosum to record ICP. The cavernous nerves were stimulated directly using a bipolar stainless-steel hook-shaped electrode with a voltage of 6 V (or 8 V for male Bama pigs), a frequency of 25 Hz and a pulse width of 2 ms. All data were visualized using the BL420N Biological Signal Recording and Analyzing System (Techman). To prevent coagulation, 50 IU of heparinized saline was added to the tube.

Construction of the full biomimetic penis

The full biomimetic penis model was mainly composed of the BCC, the biomimetic corpus spongiosum (BCS) and the biomimetic glans of the penis (BGP). The BCS and BGP were both composed of a bulbous sinus cavity (radius (*R*) = 0.6 mm in the BCS, *R* = 0.75 mm in the BGP) connected by ducts (*R* = 0.3 mm in the BCS and BGP) and the urethra (*R* = 0.6 mm in the BCS, *R* (maximum) = 0.8 mm, *R* (minimum) = 0.375 mm in the BGP). The sinus cavity and urethra in the BCS were connected with the corresponding parts in the BGP. For the BCC, we used the same structural design as in the v.2.0 BCC model and adjusted the overall proportions appropriately (the *x*, *y* and *z* axes were proportionally reduced to 75% of those used in the v.2.0 BCC model). Each part of the full biomimetic penis model was constructed with the same printing parameters and printing inks as those used to construct the BCC model, and the different components were then assembled. To facilitate the observation of the pipeline structure inside the model, we perfused the biomimetic urethral structure with blue microfil and the remaining pipeline structure with red microfil.

Preparation of the cavernous repair model

To evaluate the biocompatibility of the model materials, we performed culture experiments using hydrogel matrix conditioned medium with HUVECs and IHASMCs. HUVECs (CTCC-0804-PC) and IHASMCs (CTCC-001-0577) were obtained from the Meisen Chinese Tissue Culture Collections (Zhejiang, China). HUVECs were verified by CD31 expression analysis. IHASMCs were authenticated using short tandem repeat profiling. The cavernous repair model was constructed using the same hydrogel material and partial structure as the BCC model with dimensions of 2.0 × 1.8 × 1.0 mm (length, width and thickness), and its inner channels were connected with spherical cavities (650 μm) and cylindrical pipes (300 μm).

We treated the model surface with heparin to prevent coagulation. Surface heparinization was achieved through layer-by-layer self-assembly of poly-L-lysine (PLL) and heparin, alternating between 1 mg ml^{-1} PLL and 10 mg ml^{-1} heparin solutions (30 min each, 4 cycles) with intermittent water rinses (Supplementary Fig. 4a).

Seeding of cells within model channels

Pig and rabbit ECs were obtained from Meisen Chinese Tissue Culture Collections, isolated and expanded from corpus cavernosum following established protocols[8]. Briefly, corpus cavernosum tissue was collected aseptically, cut into 1–2-mm fragments and cultured in gelatin-coated culture dishes with endothelial cell growth medium at 37 °C and 5% CO_2. ECs were identified by von Willebrand factor (vWF) immunofluorescence staining and expanded for 3–7 passages.

To seed cells on the inner wall of the model channels, lentivirus-labelled fluorescent ECs were inoculated into the model channels at 1×10^7 cells per ml. The models were incubated for 1 h to allow cell adhesion, then flipped 180° and incubated for another hour to achieve circumferential cell attachment. Non-adherent cells were removed using fresh culture medium for incubation.

Treatment of cavernous injury in rabbit and pig models

All animal surgeries were reviewed and approved by the Animal Ethics and Welfare Committee of Guangzhou Huateng Biomedical Technology (Protocol No. HTSW220717) or the Animal Ethics and Welfare Committee of Guangdong Institute of Advanced Biomaterials and Medical Devices (Protocol Nos. IBMD23032, IBMD24011, IBMD24014), and followed the Guidelines for the Care and Use of Laboratory Animals of the National Institutes of Health.

New Zealand rabbits (40) were obtained from Guangzhou Xinhua (male, 2.5–3.5 kg, 6 months old). Cavernous injury models were established in 30 rabbits. Bama pigs (28) were obtained from Guangdong Mingzhu Biotechnology (male, 28–30 kg, 6 months old). Cavernous injury models were established in 21 pigs. The animals of each species were randomly divided into 4 experimental groups ($n = 10$ rabbits per group; $n = 7$ Bama pigs per group): implantation (models without cells), ECs + implantation (models seeded with ECs), defect (sutured without implantation) and normal. For rabbits, 5 samples per group were collected at week 4 and the remaining 5 at week 12. Similarly, for Bama pigs, 3 samples per group were collected at week 4 and 4 at week 8. Under anaesthesia, a 2 × 2 × 1 mm defect was created in the corpus cavernosum after exposing the tunica albuginea. For the defect group, only the incision was sutured without implantation. For the ECs + implantation group, the model seeded with ECs was implanted after 5 days of in vitro culture, with cyclosporine A administered post surgery (10 mg kg^{-1} day^{-1} for rabbits, 20 mg kg^{-1} day^{-1} for pigs). No operation was performed for the normal group.

For the rabbit model, evaluations included MRI scans (4 and 12 weeks post implantation), cavernous nerve electrical stimulation with ICP/MAP measurements[46,47] (12 weeks post implantation) and histological analysis (H&E staining and CD31 immunofluorescence staining). Mating studies were conducted at 10 weeks ($n = 5$ rabbits per group, 1:1 male-to-female ratio, 2-week duration).

For the pig model, at 2 weeks post surgery, all groups were subjected to electrical stimulation of the cavernous nerves to simulate an erection, and the erection morphology was captured via dual camera

positions arranged orthogonally. Blood flow during erection was characterized via colour Doppler ultrasound. The pigs were euthanized at either 4 or 8 weeks post operation, and penile tissue samples were collected from all 4 groups. Histological analyses, including H&E and Masson staining, were performed on the corpus cavernosum samples from all groups. Seven weeks after the operation, each group ($n = 4$ pigs) was paired with female pigs (6 months old) at a 1:1 male-to-female ratio and housed together for a period of 1 week. Five weeks after the mating experiment, the pregnancy status of the female pigs was observed via B-mode ultrasound, allowing non-invasive assessment. The female pigs and their offspring were not euthanized after the experiment.

MRI

MRI T2 sequences were used to evaluate the repair effect on rabbit and pig cavernous structures. After anaesthesia, a mixture of papaverine hydrochloride (30 mg ml^{-1}) and phentolamine (0.5 mg ml^{-1}) was injected into the root of the corpus cavernosum of the penis at 0.15 ml per rabbit and 1.0 ml per pig. After waiting for 5–10 min, the penis slowly became engorged with blood. Then, the animals were examined using MRI T2 sequences (Ingenia 3.0T, Philips).

Live imaging

For the pig model, at 4 and 8 weeks after surgery, the pigs in the ECs + implantation group were euthanized, and the penile tissues were obtained and immediately transferred to a live imaging system (IVIS Lumina III, PerkinElmer) for imaging with an excitation wavelength of 580 nm and an emission wavelength of 620 nm. For the rabbit model, at 4 and 12 weeks after surgery, the rabbits in the ECs + implantation group were euthanized, and the penile tissues were removed and immediately transferred to a live imaging system (AniView100, BLT) for imaging with an excitation wavelength of 580 nm and an emission wavelength of 620 nm.

Immunofluorescence staining

The samples (frozen sections or other cell samples) were fixed in 4% paraformaldehyde solution for 10 min and washed three times with PBS; then, the samples were treated with QuickBlock blocking buffer (P0260, Beyotime) for 10 min. After that, the samples were incubated with anti-CD31 (1:200 dilution, Proteintech, 11265-1-AP) at 4 °C overnight. Afterwards, the samples were washed three times with PBS and incubated with fluorescent secondary antibodies (1:500 dilution, Proteintech) at room temperature for 1 h. Then, the samples were incubated with DAPI for 10 min at room temperature and observed under a Zeiss LSM 980 confocal microscope.

RNA sequencing

The total cellular RNA of the porcine penis corpus cavernosum tissues from the implantation group, the ECs + implantation group, the control group and the normal group were sequenced using Annoroad on the NovaSeq 6000 platform. We performed comparative analyses of the sequencing results from the 4 groups.

Statistical analysis

All experiments were repeated at least three times. Data are shown as mean ± s.d. ($n \geq 3$) and were analysed with GraphPad Prism 8 software ($^{NS}P > 0.05$, $^{*}P < 0.05$, $^{**}P < 0.01$, $^{***}P < 0.001$, $^{****}P < 0.0001$).

Reporting summary

Further information on research design is available in the Nature Portfolio Reporting Summary linked to this article.

Data availability

The main data supporting the results in this study are available within the paper and its Supplementary Information. The RNA-sequencing data have been deposited in the Gene Expression Omnibus (GEO) under accession number GSE286369. The data generated during the study, including source data for the figures, are available from figshare at https://doi.org/10.6084/m9.figshare.28218347 (ref. 48).

References

1. Rafii, S., Butler, J. M. & Ding, B. S. Angiocrine functions of organ-specific endothelial cells. *Nature* **529**, 316–325 (2016).
2. Weaver, J. D. et al. Vasculogenic hydrogel enhances islet survival, engraftment, and function in leading extrahepatic sites. *Sci. Adv.* **3**, e1700184 (2017).
3. Ghesquiere, B., Wong, B. W., Kuchnio, A. & Carmeliet, P. Metabolism of stromal and immune cells in health and disease. *Nature* **511**, 167–176 (2014).
4. Carmeliet, P. & Jain, R. K. Molecular mechanisms and clinical applications of angiogenesis. *Nature* **473**, 298–307 (2011).
5. O'Connor, C., Brady, E., Zheng, Y., Moore, E. & Stevens, K. R. Engineering the multiscale complexity of vascular networks. *Nat. Rev. Mater.* **7**, 702–716 (2022).
6. Andersson, K. E. Pharmacology of penile erection. *Pharmacol. Rev.* **53**, 417–450 (2001).
7. Yafi, F. A. et al. Erectile dysfunction. *Nat. Rev. Dis. Primers* **2**, 16003 (2016).
8. Chen, K. L., Eberli, D., Yoo, J. J. & Atala, A. Bioengineered corporal tissue for structural and functional restoration of the penis. *Proc. Natl Acad. Sci. USA* **107**, 3346–3350 (2010).
9. Goldstein, I. et al. Oral sildenafil in the treatment of erectile dysfunction. *N. Engl. J. Med.* **338**, 1397–1404 (1998).
10. Burnett, A. L., Lowenstein, C. J., Bredt, D. S., Chang, T. S. & Snyder, S. H. Nitric oxide: a physiologic mediator of penile erection. *Science* **257**, 401–403 (1992).
11. Udelson, D., L'Esperance, J., Morales, A. M., Patel, R. & Goldstein, I. The mechanics of corporal veno-occlusion in penile erection: a theory on the effect of stretch-associated luminal constrictability on outflow resistance. *Int. J. Impot. Res.* **12**, 315–327 (2000).
12. Bosch, R. J. et al. Penile detumescence: characterization of three phases. *J. Urol.* **146**, 867–871 (1991).
13. Chai, M. et al. Bionic artificial penile tunica albuginea. *Matter* **6**, 626–641 (2023).
14. Gundogdu, G. et al. Evaluation of bi-layer silk fibroin grafts for penile tunica albuginea repair in a rabbit corporoplasty model. *Front. Bioeng. Biotechnol.* **9**, 791119 (2021).
15. Gelbard, M. K., Dorey, F. & James, K. The natural history of Peyronie's disease. *J. Urol.* **144**, 1376–1379 (1990).
16. Kadioglu, A. et al. A retrospective review of 307 men with Peyronie's disease. *J. Urol.* **168**, 1075–1079 (2002).
17. Dibenedetti, D. B., Nguyen, D., Zografos, L., Ziemiecki, R. & Zhou, X. A population-based study of Peyronie's disease: prevalence and treatment patterns in the United States. *Adv. Urol.* **2011**, 282503 (2011).
18. Chen, J., Gefen, A., Greenstein, A., Matzkin, H. & Elad, D. Predicting penile size during erection. *Int. J. Impot. Res.* **12**, 328–333 (2000).
19. Lee, A. et al. 3D bioprinting of collagen to rebuild components of the human heart. *Science* **365**, 482–487 (2019).
20. Grigoryan, B. et al. Multivascular networks and functional intravascular topologies within biocompatible hydrogels. *Science* **364**, 458–464 (2019).
21. Kuang, X. et al. Grayscale digital light processing 3D printing for highly functionally graded materials. *Sci. Adv.* **5**, eaav5790 (2019).
22. Wetterauer, U. in *Sexology* (eds Eicher, W. et al.) 115–126 (Springer, 1988).
23. Jang, K. I. et al. Soft network composite materials with deterministic and bio-inspired designs. *Nat. Commun.* **6**, 6566 (2015).

24. Pritchard, R. H., Huang, Y. Y. & Terentjev, E. M. Mechanics of biological networks: from the cell cytoskeleton to connective tissue. *Soft Matter* **10**, 1864–1884 (2014).
25. Onck, P. R., Koeman, T., van Dillen, T. & van der Giessen, E. Alternative explanation of stiffening in cross-linked semiflexible networks. *Phys. Rev. Lett.* **95**, 178102 (2005).
26. Meyers, M. A., McKittrick, J. & Chen, P. Y. Structural biological materials: critical mechanics-materials connections. *Science* **339**, 773–779 (2013).
27. Veale, D., Miles, S., Bramley, S., Muir, G. & Hodsoll, J. Am I normal? A systematic review and construction of nomograms for flaccid and erect penis length and circumference in up to 15,521 men. *BJU Int.* **115**, 978–986 (2015).
28. Chen, X. B., Li, R. X., Yang, H. N. & Dai, J. C. A comprehensive, prospective study of penile dimensions in Chinese men of multiple ethnicities. *Int. J. Impot. Res.* **26**, 172–176 (2014).
29. de Meyer, J. M. & Thibo, P. The correlation among cavernous pressure, penile rigidity and resistance index. *J. Urol.* **160**, 63–66 (1998).
30. Mudau, M., Genis, A., Lochner, A. & Strijdom, H. Endothelial dysfunction: the early predictor of atherosclerosis. *Cardiovasc. J. Afr.* **23**, 222–231 (2012).
31. de Meyer, J. M. & Thibo, P. The effect of re-dosing of vasodilators on the intracavernosal pressure and on the penile rigidity. *Eur. Urol.* **33**, 293–296 (1998).
32. Zhang, Y. S. & Khademhosseini, A. Advances in engineering hydrogels. *Science* **356**, eaaf3627 (2017).
33. Yuk, H. et al. Dry double-sided tape for adhesion of wet tissues and devices. *Nature* **575**, 169–174 (2019).
34. An, G. et al. Functional reconstruction of injured corpus cavernosa using 3D-printed hydrogel scaffolds seeded with HIF-1α-expressing stem cells. *Nat. Commun.* **11**, 2687 (2020).
35. Zhao, X. et al. Photocrosslinkable gelatin hydrogel for epidermal tissue engineering. *Adv. Healthc. Mater.* **5**, 108–118 (2016).
36. Chiappone, A. et al. 3D printed PEG-based hybrid nanocomposites obtained by sol-gel technique. *ACS Appl. Mater. Interfaces* **8**, 5627–5633 (2016).
37. Kim, S. H. et al. Precisely printable and biocompatible silk fibroin bioink for digital light processing 3D printing. *Nat. Commun.* **9**, 1620 (2018).
38. Wu, Y., Chee, A. J. Y., Golzar, H., Yu, A. C. H. & Tang, X. Embedded 3D printing of ultrasound-compatible arterial phantoms with biomimetic elasticity. *Adv. Funct. Mater.* **32**, 2110153 (2022).
39. Bakarich, S. E., Panhuis, M. I. H., Beirne, S., Wallace, G. G. & Spinks, G. M. Extrusion printing of ionic-covalent entanglement hydrogels with high toughness. *J. Mater. Chem. B* **1**, 4939–4946 (2013).
40. Tavafoghi, M. et al. Engineering tough, injectable, naturally derived, bioadhesive composite hydrogels. *Adv. Healthc. Mater.* **9**, 1901722 (2020).
41. Ge, Q. et al. 3D printing of highly stretchable hydrogel with diverse UV curable polymers. *Sci. Adv.* **7**, eaba4261 (2021).
42. Kim, D. H. et al. Epidermal electronics. *Science* **333**, 838–843 (2011).
43. Wang, S. et al. Skin electronics from scalable fabrication of an intrinsically stretchable transistor array. *Nature* **555**, 83–88 (2018).
44. Jones, T. J., Jambon-Puillet, E., Marthelot, J. & Brun, P. T. Bubble casting soft robotics. *Nature* **599**, 229–233 (2021).
45. Kwon, T. G., Yoo, J. J. & Atala, A. Autologous penile corpora cavernosa replacement using tissue engineering techniques. *J. Urol.* **168**, 1754–1758 (2002).
46. Fandel, T. M. et al. Recruitment of intracavernously injected adipose-derived stem cells to the major pelvic ganglion improves erectile function in a rat model of cavernous nerve injury. *Eur. Urol.* **61**, 201–210 (2012).
47. Ferretti, L. et al. Tissue engineering for penile surgery: comparative study of noncellular and cell-seeded synthetic grafts for tunica albuginea replacement. *J. Sex. Med.* **9**, 625–631 (2012).
48. Wang, Z. & Liu, X. Data for 3D-printed perfused models of the penis for the study of penile physiology and for restoring erectile function in rabbits and pigs. *figshare* https://doi.org/10.6084/m9.figshare.28218347 (2025).

Acknowledgements

We thank Q. Zhang for providing technical assistance and M. Chai for participating in helpful discussions. Y.W. discloses support for the research described in this study from the National Natural Science Foundation of China (grant number T2288101). X.S. discloses support for the publication of this study from the National Natural Science Foundation Joint Fund of China (grant number U22A20157). X.L. discloses support for the publication of this study from the National Natural Science Foundation of China (grant no. 32301136 to X.L.).

Author contributions

K.W.L., Y.W. and X.S. conceived the project. Z.W., X.L., T.Y. and Z.Z. designed and performed most of the experiments. D.S., K.W., Y.K. and S.O. conducted experimental investigations and analysed the data. Z.W. and X.L. wrote the original draft. K.W.L., Y.W. and X.S. supervised the work and revised the paper. All authors reviewed and approved the final version of the paper.

Competing interests

The authors declare no competing interests.

Additional information

Extended data is available for this paper at https://doi.org/10.1038/s41551-025-01367-y.

Supplementary information The online version contains supplementary material available at https://doi.org/10.1038/s41551-025-01367-y.

Correspondence and requests for materials should be addressed to Yingjun Wang, Kam W. Leong or Xuetao Shi.

Peer review information *Nature Biomedical Engineering* thanks Andres Garcia, Petra de Graaf, Ji Liu, Y. Shrike Zhang and the other, anonymous, reviewer(s) for their contribution to the peer review of this work.

https://doi.org/10.1038/s41551-025-01367-y

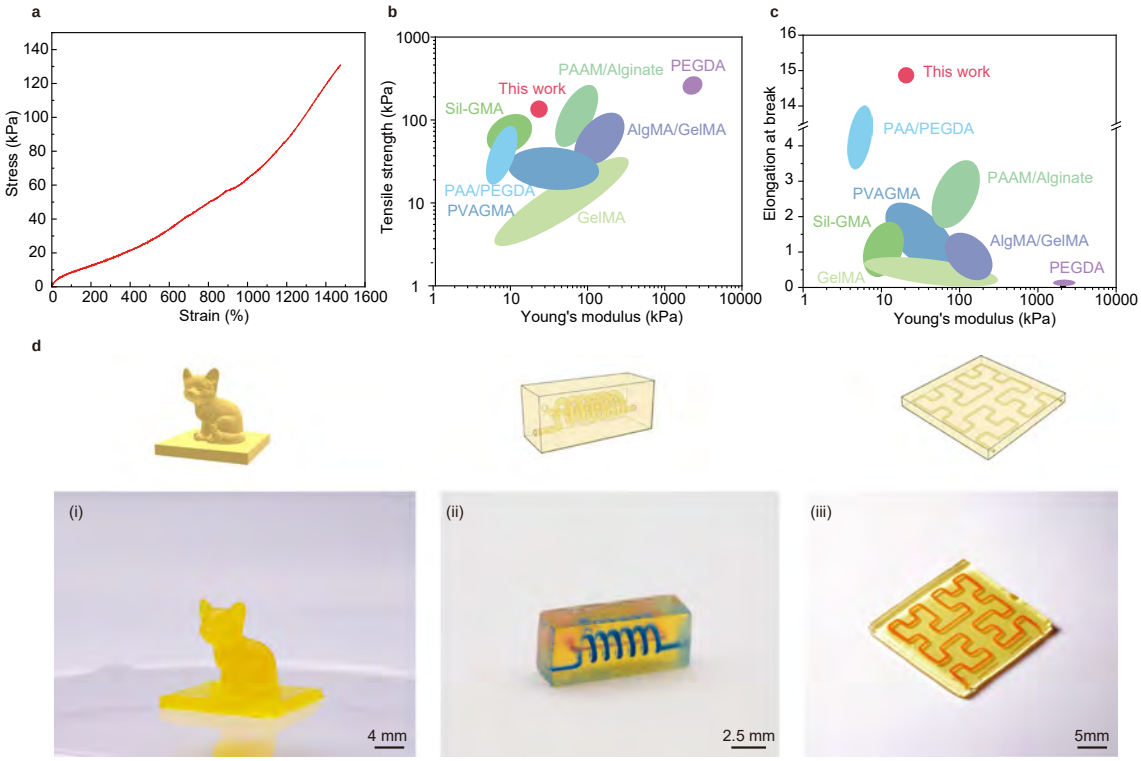

Extended Data Fig. 1 | The mechanical tensile properties and 3D printing results of the hydrogels prepared in this study. a, The stress–strain curve of the hydrogel. **b**-**c**, Ashby chart of the mechanical properties for various 3D-printed hydrogels, tensile strength versus Young's modulus (**b**) and elongation at break versus Young's modulus (**c**). Hydrogels include the hydrogel prepared in this work (red area), gelatin methacryloyl (GelMA)[35], polyethylene glycol diacrylate (PEGDA)[36], glycidyl methacrylated silk fibroin (Sil-GMA)[37], glycidyl methacrylated poly (vinyl alcohol) (PVAGMA)[38], polyacrylamide (PAAm)/Alginate[39], methacrylate-modified alginate (AlgMA)/GelMA[40], and polyacrylic acid (PAA)/PEGDA[41]. **d**, Various 3D printing models of the hydrogel, including a fox (i), axial vessel and helix (ii) and a Hilbert microchannel (iii).

https://doi.org/10.1038/s41551-025-01367-y

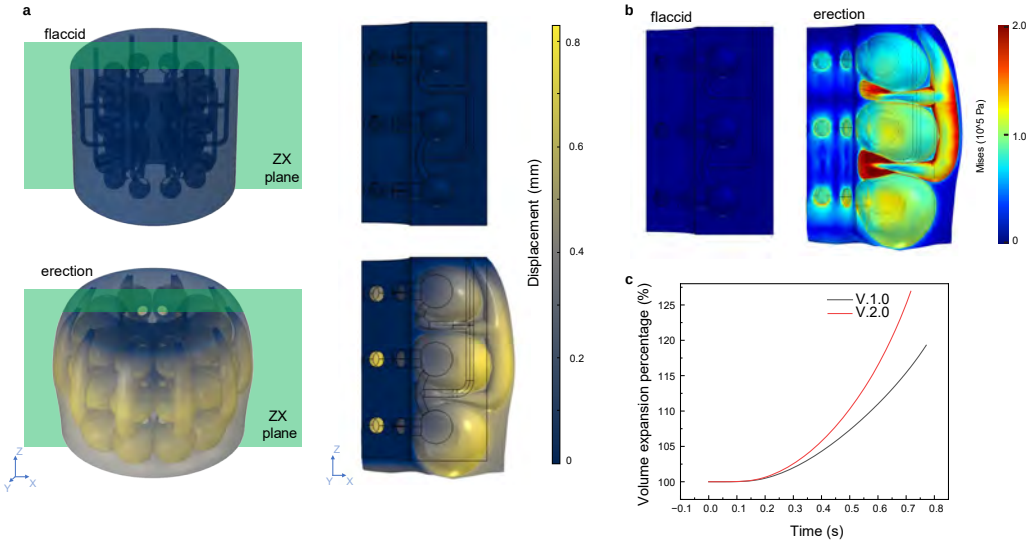

Extended Data Fig. 2 | Numerical simulation of the BCC models. **a-b**, Displacement maps (**a**) and von Mises stress maps (**b**) show that the V.1.0 BCC model can achieve venous occlusion during erection. The height and diameter of the flaccid model in the numerical simulation are 9.6 mm and 16 mm, respectively. **c**, Time–volume expansion curve, showing that the V.2.0 BCC model exhibits faster erectile deformation than the V.1.0 BCC model.

https://doi.org/10.1038/s41551-025-01367-y

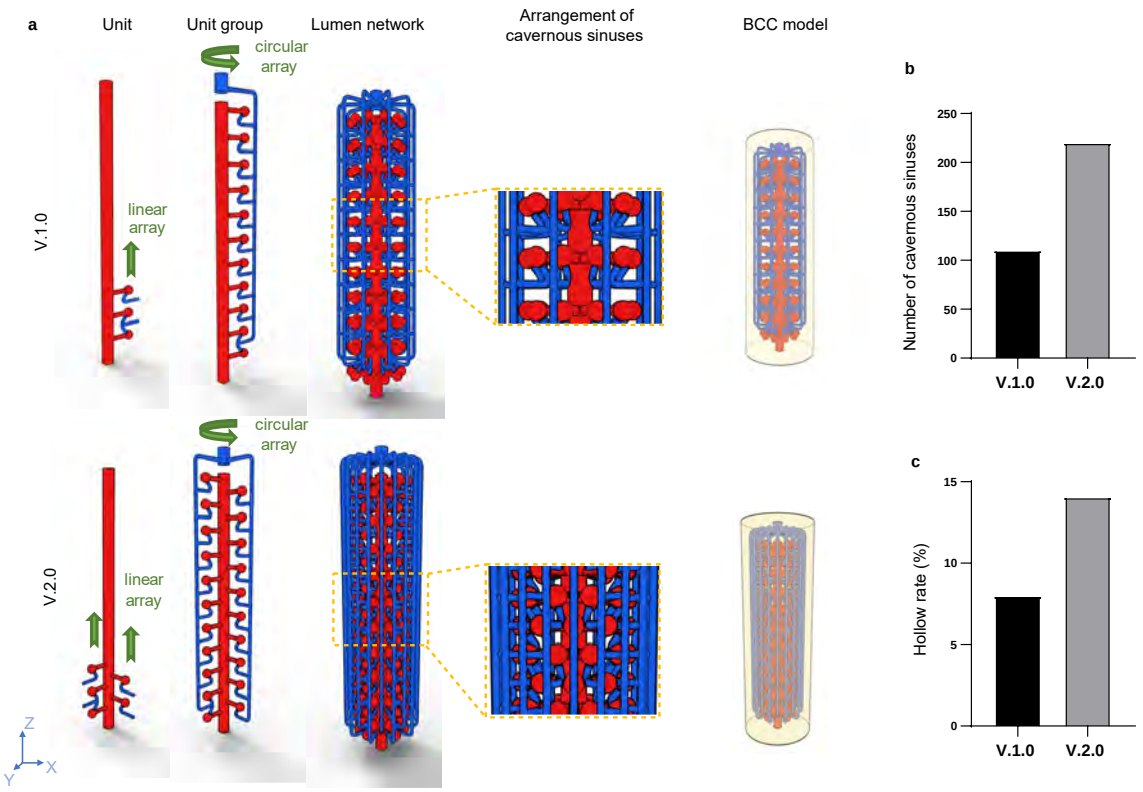

Extended Data Fig. 3 | Schematic diagram of the structural design of the BCC models. a, Procedural derivation of the two versions of the BCC models from the structural units. **b**, Statistics for the numbers of cavernous sinuses in the different versions of the BCC models. **c**, Statistics for the hollow rates of the different versions of BCC models.

https://doi.org/10.1038/s41551-025-01367-y

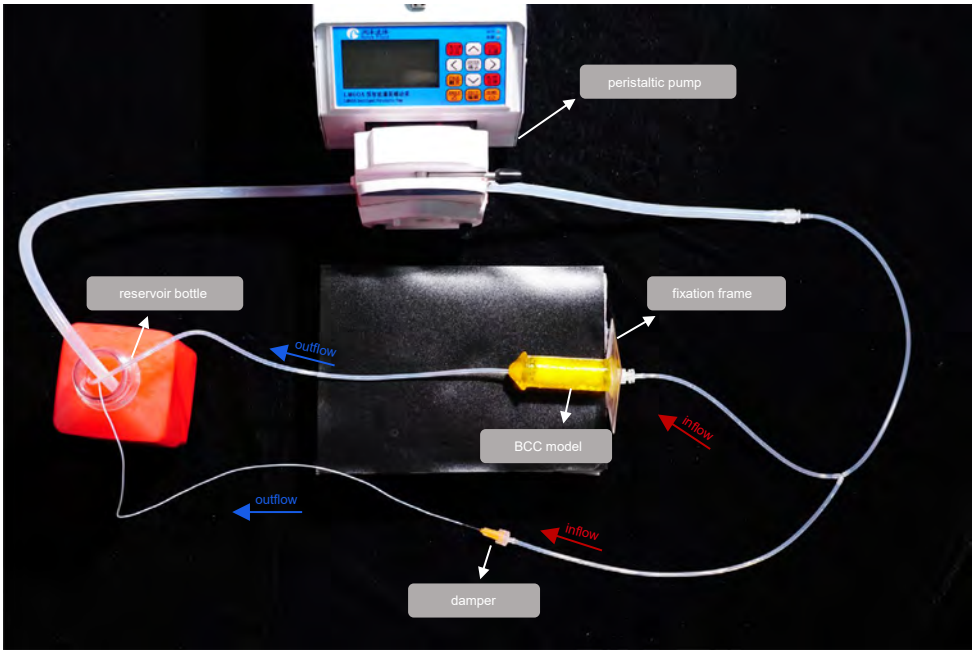

Extended Data Fig. 4 | Perfusion device for all the models (including the BCC, BCC with the wrapped biomimetic tunica albuginea, ED, and PD models). The fixation frame ensures that the model remains stable during perfusion.

https://doi.org/10.1038/s41551-025-01367-y

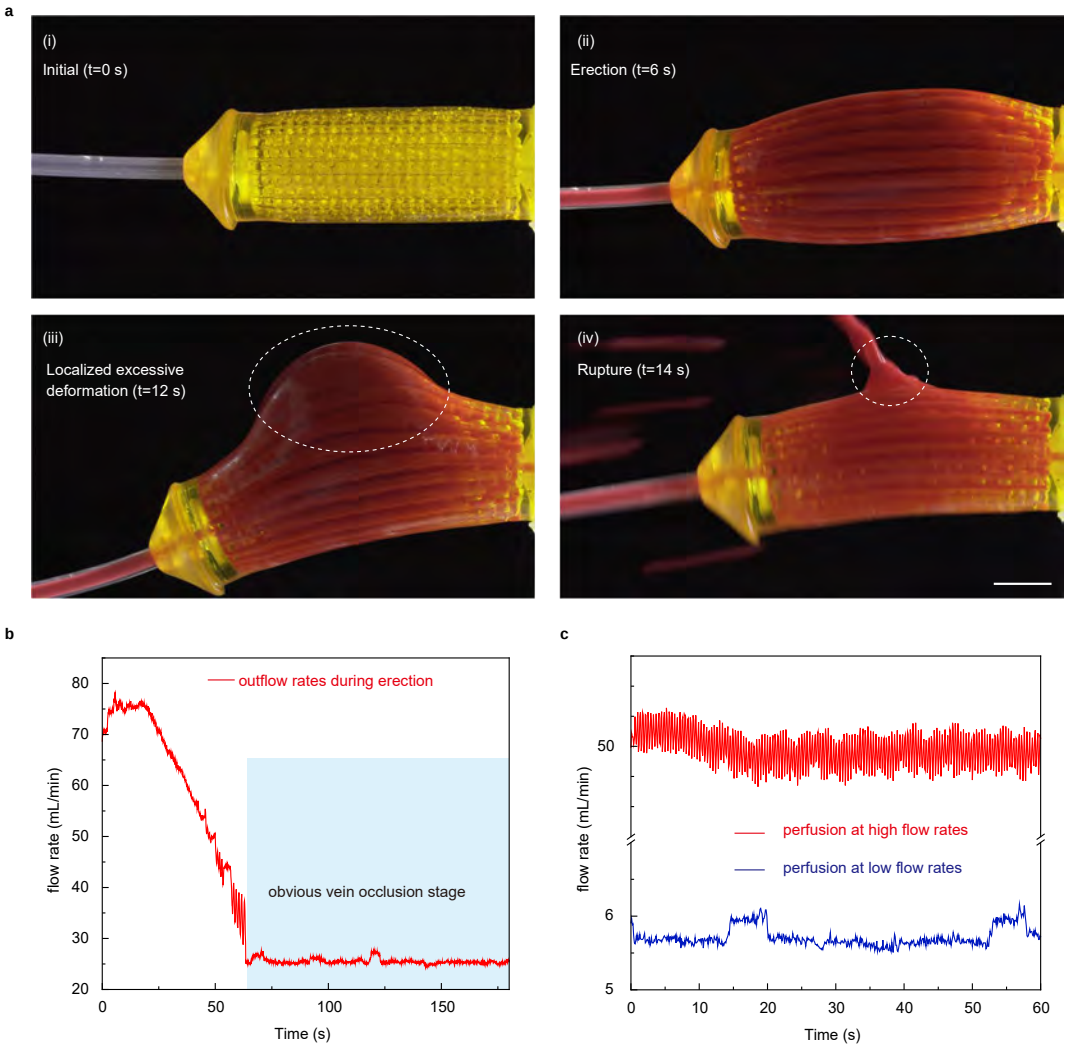

Extended Data Fig. 5 | Local deformation to damage and flow measurement. **a**, During perfusion (average flow, 90 mL/min), the BCC model exhibited notable local deformation without the constraint imposed by the biomimetic tunica albuginea. As a result, the BCC model suffers from local damage (scale bar: 9 mm). **b**, The outflow rate changes over time during *in vitro* erection perfusion in the BCC model wrapped with biomimetic tunica albuginea. The decrease in outlet flow caused by vein occlusion can be clearly observed. The blue shaded area indicates the venous occlusion state during BCC perfusion erection. **c**, Inflow rate of the ED model under high and low perfusion flow rates.

https://doi.org/10.1038/s41551-025-01367-y

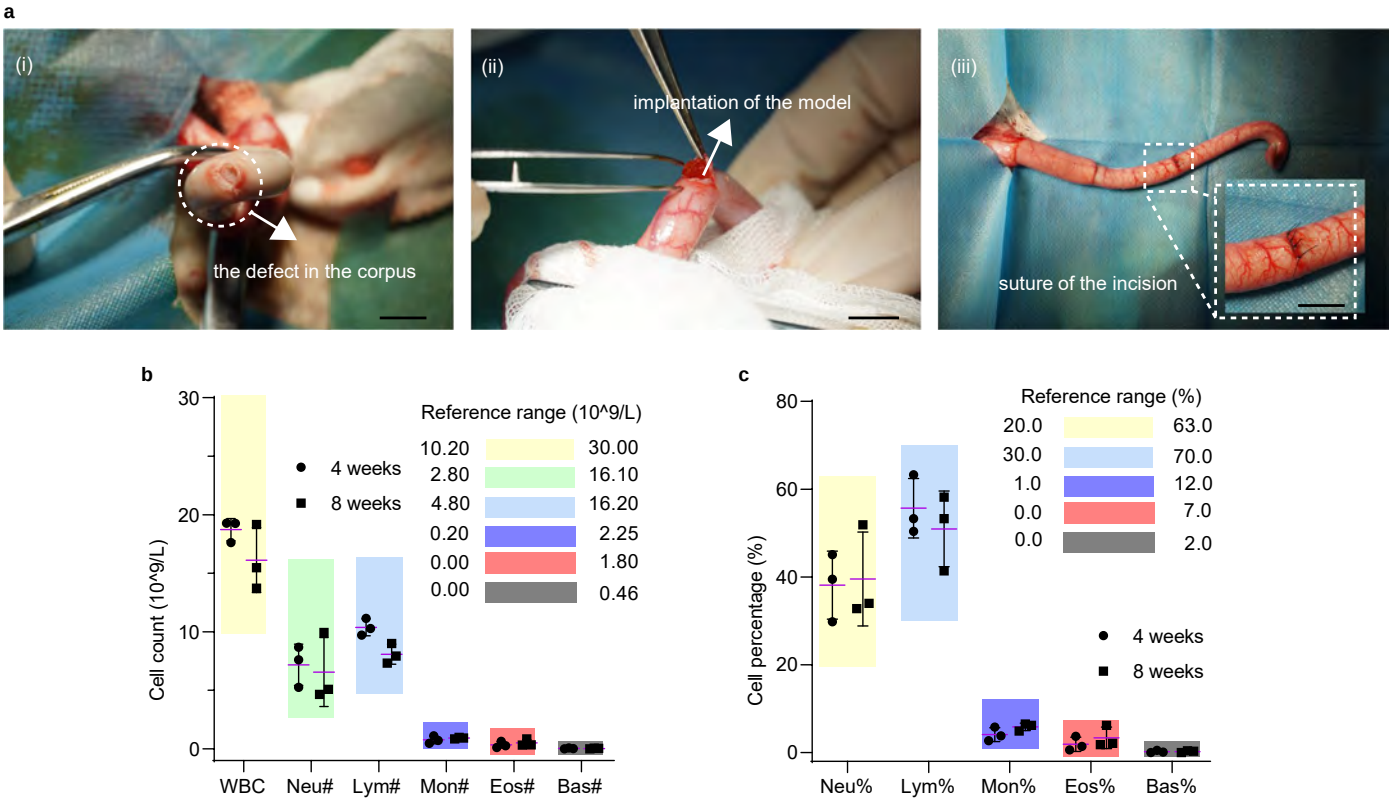

Extended Data Fig. 6 | Implantation of the hydrogel model into the porcine corpus cavernosum. a, Surgical procedure for implanting the model into the corpus cavernosum defect site (scale bar: 10 mm). **b-c**, Routine blood test results for the samples obtained from pigs implanted with the hydrogel model, including the cell count index (**b**) and the cell percentage index (**c**) (scale bar: 10 mm).

https://doi.org/10.1038/s41551-025-01367-y

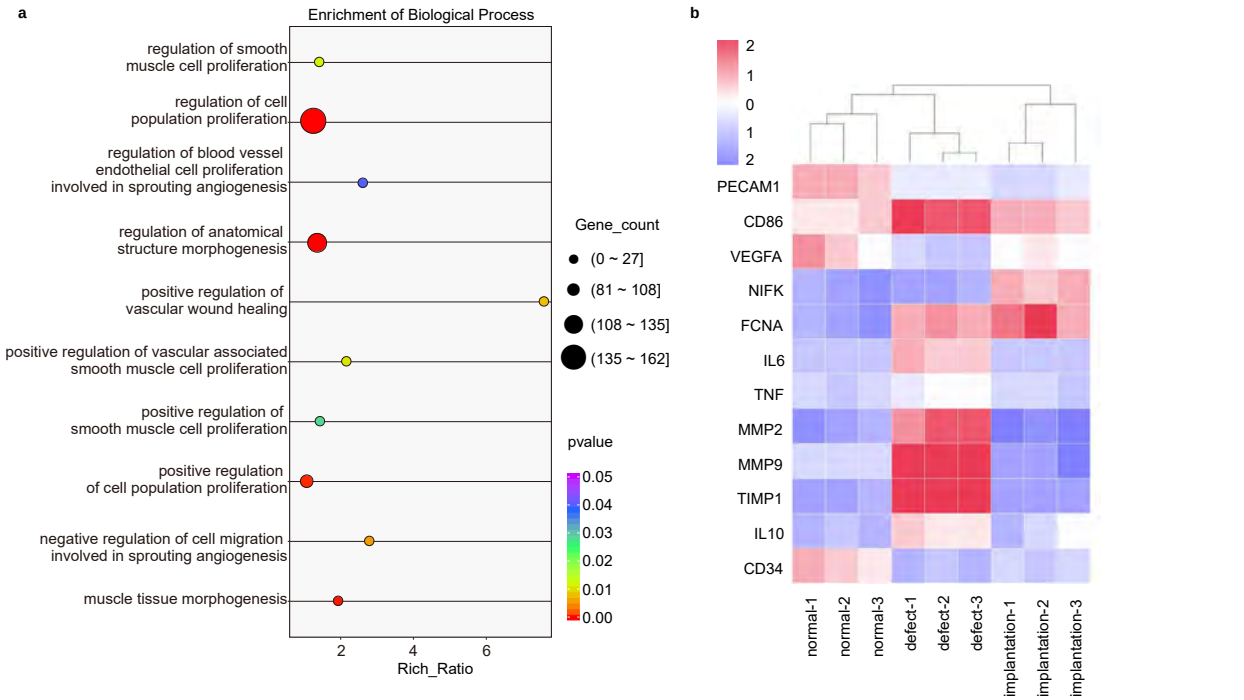

Extended Data Fig. 7 | RNA sequencing. a, Enriched Gene Ontology (GO) terms in the upregulated proliferation-related genes of the porcine penis corpus cavernosum tissues from the implantation group versus the normal group (n = 3 pigs). The statistical analysis was performed using one-side hypergeometric test. **b**, Heatmap showing the differences in the expression of proliferation-related genes and inflammation-related genes among the three different groups (normal, defect and implantation groups). The color key from red to blue represents high to low gene expression levels, respectively (n = 3 pigs). Statistical analysis was performed using two-sided One-way ANOVA followed by Tukey's multiple comparison test. Data are presented as mean ± SD (n = 3 pigs).

nature portfolio

Corresponding author(s): Kam Leong

Last updated by author(s): Jan 12, 2025

Reporting Summary

Nature Portfolio wishes to improve the reproducibility of the work that we publish. This form provides structure for consistency and transparency in reporting. For further information on Nature Portfolio policies, see our Editorial Policies and the Editorial Policy Checklist.

Statistics

For all statistical analyses, confirm that the following items are present in the figure legend, table legend, main text, or Methods section.

n/a	Confirmed
☐	☒ The exact sample size (*n*) for each experimental group/condition, given as a discrete number and unit of measurement
☐	☒ A statement on whether measurements were taken from distinct samples or whether the same sample was measured repeatedly
☐	☒ The statistical test(s) used AND whether they are one- or two-sided *Only common tests should be described solely by name; describe more complex techniques in the Methods section.*
☐	☒ A description of all covariates tested
☒	☐ A description of any assumptions or corrections, such as tests of normality and adjustment for multiple comparisons
☐	☒ A full description of the statistical parameters including central tendency (e.g. means) or other basic estimates (e.g. regression coefficient) AND variation (e.g. standard deviation) or associated estimates of uncertainty (e.g. confidence intervals)
☐	☒ For null hypothesis testing, the test statistic (e.g. *F*, *t*, *r*) with confidence intervals, effect sizes, degrees of freedom and *P* value noted *Give P values as exact values whenever suitable.*
☒	☐ For Bayesian analysis, information on the choice of priors and Markov chain Monte Carlo settings
☒	☐ For hierarchical and complex designs, identification of the appropriate level for tests and full reporting of outcomes
☒	☐ Estimates of effect sizes (e.g. Cohen's *d*, Pearson's *r*), indicating how they were calculated

Our web collection on statistics for biologists contains articles on many of the points above.

Software and code

Policy information about availability of computer code

Data collection	The Uniaxial tensile tests were performed using a universal testing machine (Instron 5967, Instron, USA). The dynamic mechanics analyzer (Q800, TA, USA) was utilized for the cyclic loading–unloading tensile tests. Photorheological characterization was performed using a rheometer (Discovery HR-2, TA, USA). BL-420 N physiometer (Techman, Chengdu, China) was used for ICP test. The total cellular RNAs of the porcine penis corpus cavernosum tissues were sequenced by Annoroad on the NovaSeq 6000 platform.
Data analysis	GraphPad Prism 8 was used for the generation of graphs and for data analysis. ImageJ v1.51j8 software (National Institutes of Health, USA) was used for the quantization of images. Blender (v3.1) was used for three-dimensional modeling. COMSOL Multiphysics (v5.6) was used for numerical simulations. Micro-CT reconstruction and analysis were performed using Mimics Medical software (v21.0).

For manuscripts utilizing custom algorithms or software that are central to the research but not yet described in published literature, software must be made available to editors and reviewers. We strongly encourage code deposition in a community repository (e.g. GitHub). See the Nature Portfolio guidelines for submitting code & software for further information.

Data

Policy information about availability of data

All manuscripts must include a data availability statement. This statement should provide the following information, where applicable:

- Accession codes, unique identifiers, or web links for publicly available datasets
- A description of any restrictions on data availability
- For clinical datasets or third party data, please ensure that the statement adheres to our policy

The main data supporting the results in this study are available within the paper and its Supplementary Information. The RNA-sequencing data have been deposited in the Gene Expression Omnibus (GEO) under accession number GSE286369. The data generated during the study, including source data for the figures, are available from figshare with the identifier https://doi.org/10.6084/m9.figshare.28190399.

Research involving human participants, their data, or biological material

Policy information about studies with human participants or human data. See also policy information about sex, gender (identity/presentation), and sexual orientation and race, ethnicity and racism.

Reporting on sex and gender	The study did not involve human participants nor human data.
Reporting on race, ethnicity, or other socially relevant groupings	–
Population characteristics	–
Recruitment	–
Ethics oversight	–

Note that full information on the approval of the study protocol must also be provided in the manuscript.

Field-specific reporting

Please select the one below that is the best fit for your research. If you are not sure, read the appropriate sections before making your selection.

☒ Life sciences ☐ Behavioural & social sciences ☐ Ecological, evolutionary & environmental sciences

For a reference copy of the document with all sections, see nature.com/documents/nr-reporting-summary-flat.pdf

Life sciences study design

All studies must disclose on these points even when the disclosure is negative.

Sample size	We did a preliminary experiment first, and combined with previous experience and standards in the field, we then set up the number of samples in different groups.
Data exclusions	No data exclusions were made.
Replication	All the experiments were carried out in three replicates or more. All experiments were repeated successfully, with consistent results.
Randomization	The animals were randomly separated into different groups.
Blinding	Some sets of data (H&E and Masson staining analysis, pig-mating experiment, and ultrasound of embryos) were analysed with a double-blind approach. The authors measuring parameters in samples were unaware of the treatment. Blinding was not possible for mechanical-testing and model-evaluation experiments because these experiments required the direct observation and measurement of specific material properties and model-performance parameters.

Reporting for specific materials, systems and methods

We require information from authors about some types of materials, experimental systems and methods used in many studies. Here, indicate whether each material, system or method listed is relevant to your study. If you are not sure if a list item applies to your research, read the appropriate section before selecting a response.

Materials & experimental systems

n/a	Involved in the study
☐	☒ Antibodies
☐	☒ Eukaryotic cell lines
☒	☐ Palaeontology and archaeology
☐	☒ Animals and other organisms
☒	☐ Clinical data
☒	☐ Dual use research of concern
☒	☐ Plants

Methods

n/a	Involved in the study
☒	☐ ChIP-seq
☒	☐ Flow cytometry
☒	☐ MRI-based neuroimaging

Antibodies

Antibodies used	CD31 Polyclonal antibody was from Proteintech (11265-1-AP, CD31 Rabbit PloyAb, 00114609, 1:200 dilution for IF/ICC, KD/KO Validated, Applications: WB, IHC, IF/ICC, IF-P, IP, ELISA).
Validation	The specificity of antibodies used in this study was validated using knockout (KO) and/or knockdown (KD) approaches, confirming their target specificity.

Eukaryotic cell lines

Policy information about cell lines and Sex and Gender in Research

Cell line source(s)	HUVECs (CTCC-0804-PC) and IHASMCs (CTCC-001-0577) were obtained from the Meisen Chinese Tissue Culture Collections (Zhejiang, China).
Authentication	For HUVECs, CD31 expression was evaluated for authentication. For IHASMCs, the cell line was authenticated using short-tandem-repeat analysis. For rabbit corpus cavernosum ECs and pig corpus cavernosum ECs, the expression of vwf was evaluated for authentication.
Mycoplasma contamination	There was no mycoplasma contamination.
Commonly misidentified lines (See ICLAC register)	No commonly misidentifed cell lines were used.

Animals and other research organisms

Policy information about studies involving animals; ARRIVE guidelines recommended for reporting animal research, and Sex and Gender in Research

Laboratory animals	Seven-week-old Sprague–Dawley rats (250–350 g) were obtained from Guangzhou Ruige Biotechnology Co., Ltd. Six-month-old New Zealand rabbits (2.53.5 kg), comprising 40 males and 20 females, were sourced from Guangzhou Xinhua Co., Ltd. Bama pigs (6-months-old, sexually mature), comprising 28 males and 16 females, were acquired from Guangdong Mingzhu Biotechnology Co., Ltd.
Wild animals	The study did not involve wild animals.
Reporting on sex	Because the animal experiments were to repair penile damage in male pigs, we used male rabbits and Bama pigs for repairing corpus-cavernosum defects. We used female rabbits and Bama pigs in the the mating experiment.
Field-collected samples	The study did not involve samples collected from the field.
Ethics oversight	All animal surgeries were reviewed and approved by the Animal Ethical and Welfare Committee of Guangzhou Huateng Biomedical Technology Co., Ltd. (Guangzhou, China) or the Animal Ethical and Welfare Committee of Guangdong Institute of Advanced Biomaterials and Medical Devices (Guangzhou, China), and followed the guidelines of the National Institutes of Health. The IACUC numbers are HTSW220717, IBMD23032, IBMD24011 and IBMD24014.

Note that full information on the approval of the study protocol must also be provided in the manuscript.